Consistency of cosmic shear analyses in harmonic and real space

C. Doux,[1]* C. Chang,[2,3]† B. Jain,[1] J. Blazek,[4,5] H. Camacho,[6,7] X. Fang,[8] M. Gatti,[9] E. Krause,[8]
N. MacCrann,[10] S. Samuroff,[11] L. F. Secco,[1] M. A. Troxel,[12] J. Zuntz,[13] M. Aguena,[14,7] S. Allam,[15]
A. Amon,[16] S. Avila,[17] D. Bacon,[18] E. Bertin,[19,20] D. Brooks,[21] D. L. Burke,[16,22] A. Carnero Rosell,[23,7,24]
M. Carrasco Kind,[25,26] J. Carretero,[9] A. Choi,[4] M. Costanzi,[27,28,29] M. Crocce,[30,31] L. N. da Costa,[7,32]
M. E. S. Pereira,[33] T. M. Davis,[34] J. P. Dietrich,[35] P. Doel,[21] I. Ferrero,[36] A. Ferté,[37] P. Fosalba,[30,31]
J. García-Bellido,[17] E. Gaztanaga,[30,31] D. W. Gerdes,[38,33] D. Gruen,[39,16,22] R. A. Gruendl,[25,26]
J. Gschwend,[7,32] G. Gutierrez,[15] W. G. Hartley,[40] S. R. Hinton,[34] D. L. Hollowood,[41] D. Huterer,[33]
D. J. James,[42] K. Kuehn,[43,44] N. Kuropatkin,[15] M. A. G. Maia,[7,32] J. L. Marshall,[45] F. Menanteau,[25,26]
R. Miquel,[46,9] R. Morgan,[47] A. Palmese,[15,3] F. Paz-Chinchón,[25,48] A. A. Plazas,[49] A. Roodman,[16,22]
E. Sanchez,[50] M. Schubnell,[33] S. Serrano,[30,31] I. Sevilla-Noarbe,[50] M. Smith,[51] M. Soares-Santos,[33]
E. Suchyta,[52] G. Tarle,[33] C. To,[39,16,22] T. N. Varga,[53,54] J. Weller,[53,54] and R.D. Wilkinson[55]

(DES Collaboration)

ABSTRACT

Recent cosmic shear studies have reported discrepancies of up to 1σ on the parameter $S_8 = \sigma_8 \sqrt{\Omega_m/0.3}$ between the analysis of shear power spectra and two-point correlation functions, derived from the same shear catalogs. It is not *a priori* clear whether the measured discrepancies are consistent with statistical fluctuations. In this paper, we investigate this issue in the context of the forthcoming analyses from the third year data of the Dark Energy Survey (DES-Y3). We analyze DES-Y3 mock catalogs from Gaussian simulations with a fast and accurate importance sampling pipeline. We show that the methodology for determining matching scale cuts in harmonic and real space is the key factor that contributes to the scatter between constraints derived from the two statistics. We compare the published scales cuts of the KiDS, Subaru-HSC and DES surveys, and find that the correlation coefficients of posterior means range from over 80% for our proposed cuts, down to 10% for cuts used in the literature. We then study the interaction between scale cuts and systematic uncertainties arising from multiple sources: non-linear power spectrum, baryonic feedback, intrinsic alignments, uncertainties in the point-spread function, and redshift distributions. We find that, given DES-Y3 characteristics and proposed cuts, these uncertainties affect the two statistics similarly; the differential biases are below a third of the statistical uncertainty, with the largest biases arising from intrinsic alignment and baryonic feedback. While this work is aimed at DES-Y3, the tools developed can be applied to Stage-IV surveys where statistical errors will be much smaller.

Key words: gravitational lensing: weak – cosmological parameters – large-scale structure of Universe.

1 INTRODUCTION

Weak gravitational lensing, the apparent distortion of galaxy shapes due to the intervening dark matter distribution in the line-of-sight, is one of the most powerful tools for constraining cosmological parameters at low redshift (Albrecht et al. 2006). In particular, the derived parameter $S_8 = \sigma_8 \sqrt{\Omega_m/0.3}$ points roughly to the most constraining

direction of weak lensing datasets (Jain & Seljak 1997), where σ_8 is the amplitude of structure in the Universe, parametrized as the standard deviation of the linear overdensity fluctuations in $8\,h^{-1}$ Mpc spheres at present time, and Ω_m is the density parameter of matter at present time. The primary cosmological constraints from weak lensing analyses come from two-point statistics of weak lensing distortion, referred to as cosmic shear, which may be evaluated in real (or configuration), harmonic or other spaces. The most commonly used two-point statistics in real space are the shear two-point angular correlation functions $\xi_{\pm}(\theta)$ (Hildebrandt et al. 2017; Troxel

* E-mail: cdoux@sas.upenn.edu
† E-mail: chihway@kicp.uchicago.edu

et al. 2018a; Hamana et al. 2020), whereas in harmonic space, the shear power spectrum C_ℓ of lensing E-modes (see e.g. Bartelmann & Schneider 2001, and Section 2.1 for a review of formalism) is often used (Köhlinger et al. 2017; Hikage et al. 2019). Both present advantages and drawbacks. $\xi_\pm$ measurements are insensitive to the survey geometry and straightforward to compute (Jarvis et al. 2004), but they are heavily correlated across scales (*i.e.* the covariance has large off-diagonal contributions). C_ℓ measurements, on the other hand, are typically based on a pixelization of the shear field estimated with galaxy shapes. They must be deconvolved from the survey mask (Alonso et al. 2019) and have their shape-noise contributions subtracted, but are almost uncorrelated across multipoles for large observed areas of the sky (alternatively, one may choose to forward model the effect of the mask). Fast theoretical predictions are available for both, a requirement to perform Bayesian analysis.

Even though different statistics compress the information in different ways, one may expect both statistics—$\xi_\pm$ and C_ℓ—to return reasonably close constraints on cosmological parameters when applied to the same data set. However, both the Kilo-Degree Survey (KiDS, de Jong et al. 2013; Kuijken et al. 2015) and the Hyper Suprime-Cam survey (HSC, Aihara et al. 2018a,b) have released cosmological results of the same weak lensing data using both real and harmonic statistics, and found discrepancies at the level of 0.5 to 1.5σ. In Hildebrandt et al. (2017), the authors derived the constraint $S_8 = 0.745 \pm 0.039$ based on cosmic shear measured with $\xi_\pm$ in the 450 deg^2 KiDS dataset, while Köhlinger et al. (2017) carried out an analysis using instead the C_ℓ statistic and obtained $S_8 = 0.651 \pm 0.058$. Similarly, with the first year of about 137 deg^2 of HSC data, Hamana et al. (2020) found $S_8 = 0.804^{+0.032}_{-0.029}$ using $\xi_\pm$, while Hikage et al. (2019) found $S_8 = 0.780^{+0.030}_{-0.033}$ based on C_ℓ. These discrepancies are concerning and make the comparison of weak lensing with other types of cosmological data ambiguous. Therefore, in light of the observed tensions between the value of σ_8 (or S_8) inferred from the cosmic microwave background and from large-scale structure at low redshift (e.g. MacCrann et al. 2015; Hildebrandt et al. 2017; DES Collaboration et al. 2018), it is crucial to understand the limitations and consistency of standard statistics such as $\xi_\pm$ and C_ℓ used in weak lensing. This is important for on-going weak lensing surveys, such as the Dark Energy Survey (DES, Flaugher 2005), the Kilo-Degree Survey (KiDS, de Jong et al. 2013; Kuijken et al. 2015), the Hyper Suprime-Cam survey (HSC, Aihara et al. 2018a,b), and even more so for upcoming ones, such as the Vera Rubin Observatory Legacy Survey of Space and Time (LSST, Ivezić et al. 2019), the ESA satellite Euclid (Laureijs et al. 2012) and the NASA's Nancy Grace Roman Space Telescope (Akeson et al. 2019).

In this paper we will show that scale cuts play a significant role in terms of the consistency between the two statistics. To illustrate this, we imagine, as a thought experiment, that we know the true shear field. If we were able to measure two-point statistics with infinite resolution—that is, for arbitrarily large multipoles ℓ, and arbitrarily small separation angles θ measured in infinitesimal bins—and provided we can fully characterize the likelihood of those estimators, both would capture the full *Gaussian* information. Therefore, we would expect identical, cosmic variance-limited posteriors on S_8 and other parameters, and equal estimators, denoted generically $\widehat{S_8}|_{\xi_\pm}$ and $\widehat{S_8}|_{C_\ell}$—*e.g.*, from the mean or mode of the respective posteriors. Now, if we consider a catalog of galaxy shapes sampled from the shear field, this step adds noise to our measurements, but the results should also perfectly agree between the $\xi_\pm$ and C_ℓ measurements. That is, we still expect $\widehat{S_8}|_{\xi_\pm} = \widehat{S_8}|_{C_\ell}$.

In practice, however, neither of the previous scenarios are realistic. First, the finite survey area and the density of observed (and selected) galaxies introduce respectively large- and small-scale cutoffs. Furthermore, cosmic shear analyses are inherently limited by theoretical uncertainties (*e.g.*, baryonic effects, intrinsic alignments) and observational effects that restrict the use of two-point statistic measurements at small scales—though accessible in the data—to derive constraints on cosmological parameters. The most straightforward solution is to decide on hard cuts, *i.e.* using only real-space angular bins between certain θ_{min} and θ_{max} for $\xi_\pm$, and, similarly, only multipoles between ℓ_{min} and ℓ_{max} for C_ℓ. The θ and ℓ cuts cannot, however, be directly translated because both statistics are related through a Bessel integral, see Eq. (3) below, such that a hard scale cut introduced in real space induces an *oscillatory* cut in harmonic space, and vice versa (see, *e.g.*, Huterer 2002). Therefore, realistic cosmic shear analyses must exclude different information for each statistic and we do not expect $\widehat{S_8}|_{\xi_\pm}$ and $\widehat{S_8}|_{C_\ell}$ to be equal because of the necessary scale cuts. In addition, cosmic shear two-point statistics at a fixed angular scale receive contributions from a wide range of physical scales—or Fourier modes k—stemming from the projection of the shear field along the line of sight that sums up distortions sourced by the matter density field from the sources to the observer. This is illustrated in Fig. 1, where the three panels show $d \ln X / d \ln k$ for $X = \xi_\pm(\theta), C_\ell$, *i.e.* the normalized integrand of $\xi_\pm$ and C_ℓ statistics as a function of scales k (for details, see Section 2.1). Due to this mixing of k-modes, and for a given choice of scale cuts, the estimators $\widehat{S_8}|_{\xi_\pm}$ and $\widehat{S_8}|_{C_\ell}$ from cosmic shear analyses are placing different weights on accessible k-modes. The question of consistency thus pertains, to a large extent, to the corresponding choice of scale cuts in harmonic and real space.

The problem was recently studied, in particular by the HSC and KiDS collaborations. Hamana et al. (2020), investigated the origin of the difference in their cosmological constraints from $\xi_\pm$ and C_ℓ, noting that for some parameters, such as Ω_m, the difference could be significant. To understand the problem, the authors performed the same real and harmonic-space analyses on 100 N-body simulations and found significant scatter between the constrains from $\xi_\pm$ and C_ℓ (see Fig. 19 of Hamana et al. 2020). They concluded that one potential explanation of the difference in the constraints from Hamana et al. (2020) and Hikage et al. (2019) is that the scales used in the two analyses do not match, such that the observed discrepancy could be explained by a statistical fluctuation at the $\sim 1.4\sigma$ level, based on discrepancies found in simulations. Recently, KiDS-1000 proposed and compared different statistics (Asgari et al. 2020b), in addition to the real-space two-point functions, namely band powers and COSEBIs (Complete Orthogonal Sets of E-/B-mode Integrals, see Schneider et al. 2010). The latter are based on linear combinations of thinly-binned measurements of $\xi_\pm$ weighted with specific window functions that amount to apply effective soft cuts. They similarly analyzed a number of simulations to quantify the expected differences. Finally, Lu & Haiman (2019) investigated a similar discrepancy found in cosmic shear data from the Canada-France-Hawaii Telescope Lensing Survey (Kilbinger et al. 2013; Liu et al. 2015) and identified excess power at very small scales ($\ell \gtrsim 5000$) to drive the larger value of the matter fluctuation amplitude inferred from the power spectrum.

In this paper, our goal is to examine conditions for consistency of the DES Y3 cosmic shear analysis in harmonic space and that performed in real space. For a given data set and choices of scales used in each analysis, the standard deviation of $\Delta \widehat{S_8} \equiv \widehat{S_8}|_{\xi_\pm} - \widehat{S_8}|_{C_\ell}$ over a large number of realizations of the shear field, denoted $\sigma(\Delta \widehat{S_8})$, is fixed. The more common information the two statistics probe, the
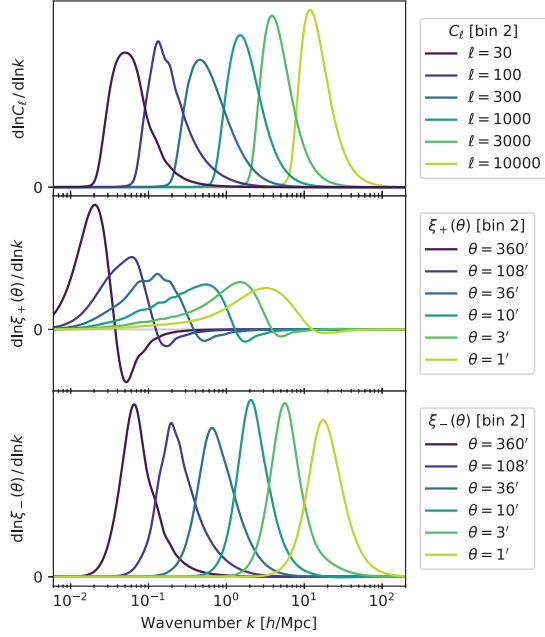
Figure 1. Contributions of physical k-modes to the shear power spectrum C_ℓ and two-point functions $\xi_\pm(\theta)$, for different multipoles ℓ and angular separations θ in the ranges used in cosmic shear analyses. These curves correspond to the integrand of the Limber formula, Eq. (1), with a change of variable $z \to k = (\ell + 1/2)/\chi(z)$. We show $\mathrm{d}\ln X/\mathrm{d}\ln k$ for $X = C_\ell, \xi_\pm(\theta)$ on a logarithmic scale in k, such that each curve is normalized to have area unity under the curve. Here, the auto-correlation for redshift bin 2 is shown (see redshift distributions and the broad lensing efficiency functions in Fig. 2).

smaller $\sigma(\widehat{\Delta S_8})$ is, and vice versa. We will measure the distribution of $(\widehat{S_8}|_{\xi_\pm}, \widehat{S_8}|_{C_\ell})$ and $\sigma(\widehat{\Delta S_8})$ from simulations of mock DES Y3 surveys, under different assumptions of noise and scale cuts. These simulations are required to accurately estimate $\widehat{\Delta S_8}$. They allow us to include the effects of cosmic variance, shape noise, and any effects coming from the particular geometry of the DES footprint. In addition, we will compare the estimated scatter of $\widehat{\Delta S_8}$ to the biases in S_8 predicted for a set of systematic effects and modeling uncertainties. Indeed, observational systematics and theoretical uncertainties in modeling are liable to impact C_ℓ and $\xi_\pm$ measurements differently depending on whether the effect has more compact support in real or harmonic space, or neither (*e.g.* for a k-dependent effect). Therefore, it is useful to measure the differential impact of systematics to the spread expected from statistical fluctuations. In order to analyze hundreds of simulations for several choices of scale cuts, we implement (and validate) an importance sampling pipeline that provides fast estimates of $\widehat{S_8}$. Finally, we will also evaluate the equivalent quantities for σ_8 and Ω_m.

This exercise is meant to provide guidance to determine scale cuts for the DES Y3 cosmic shear analysis in harmonic space. In the context of multiprobe analysis (Joudaki et al. 2018; van Uitert et al. 2018; DES Collaboration et al. 2018; Heymans et al. 2020), where one analyzes cosmic shear measurements in conjunction with galaxy clustering and galaxy-galaxy lensing measurements—*i.e.* the cross-correlation of galaxy positions and shapes—we restrict our analysis to cosmic shear. The reason is that one expects less k-mode mixing for the other two probes (at least for C_ℓ) since the integral

over redshift (or k) has limited support, given by the width of the redshift distributions of clustering galaxy samples.

The paper is structured as follows. In Section 2, we provide a brief overview of the theoretical background and we describe the baseline model used in this analysis, as well as alternative modeling choices and systematic effects for which we will examine the differential impact on harmonic *vs* real space. In Section 3 we describe several strategies in choosing scale cuts in real and harmonic space. In Section 4 we describe the generation and validation of the simulations used in this work. In Section 5 we present and validate the use of importance sampling to obtain fast estimators $\widehat{S_8}$ in both harmonic and real space. We present our estimation of $\widehat{\Delta S_8}$ in Section 6, estimate $\widehat{S_8}_{\xi_\pm} - \widehat{S_8}_{C_\ell}$ for various systematics and discuss discrepancies found in the literature. Finally, we summarize our findings in Section 7 and discuss the implications for the forthcoming DES Y3 analysis and future surveys.

2 FORMALISM AND MODELING

Our modeling of $\xi_\pm$ and C_ℓ follows closely the framework used in Krause et al. (2017) and the cosmological analysis of the first year (Y1) data of DES (Troxel et al. 2018a; DES Collaboration et al. 2018). For DES Y3, there were several improvements to this pipeline though, for the purpose of this study, the Y1 pipeline is sufficient as our simulations do not contain the higher-order corrections. We will adopt the approximate Y3 footprint with Y1 redshift distributions, shown in Fig. 2.

2.1 Theory

Here we provide the basic theoretical framework associated with the harmonic- and real-space cosmic shear two-point statistics, the power spectrum C_ℓ and two-point correlation functions $\xi_\pm$.

Under the Limber approximation (Limber 1953; Kaiser 1992, 1998; LoVerde & Afshordi 2008) and in a spatially flat Universe, the lensing power spectrum encodes cosmological information through

$$C_\ell^{ij} = \int_0^{\chi_H} \mathrm{d}\chi \frac{q^i(\chi)q^j(\chi)}{\chi^2} P_{NL}\left(k = \frac{\ell + 1/2}{\chi}, \chi\right), \quad (1)$$

where χ is the radial comoving distance, χ_H is the distance to the horizon, P_{NL} is the non-linear matter power spectrum, and $q(\chi)$ is the lensing efficiency defined via

$$q^i(\chi) = \frac{3}{2}\Omega_m \left(\frac{H_0}{c}\right)^2 \frac{\chi}{a(\chi)} \int_\chi^{\chi_H} \mathrm{d}\chi' \, n^i(\chi')\frac{\chi' - \chi}{\chi'}, \quad (2)$$

where Ω_m is the matter density today, H_0 is the Hubble parameter today, a is the scale factor, and $n^i(\chi)$ is the normalized redshift distribution of the galaxy sample i.

Assuming the flat-sky approximation (Kaiser 1992, 1998), $\xi_\pm$ and C_ℓ are connected via

$$\xi_\pm^{ij}(\theta) = \int_0^\infty \frac{\ell \, \mathrm{d}\ell}{2\pi} J_{0/4}(\theta\ell) \, C^{ij}(\ell), \quad (3)$$

where J_n is the nth-order spherical Bessel function of the first kind, with $n = 0$ ($n = 4$) for ξ_+ (ξ_-), and $C(\ell)$ is an interpolation of C_ℓ for non-integer ℓ (see Kitching et al. 2017; Lemos et al. 2017, for discussions of this approximation).

Both quantities receive contributions from the matter power spectrum over a range of physical k-modes. By applying the change of variables $k = (\ell + 1/2)/\chi(z)$ in Eq. (1) and using Eq. (3), we
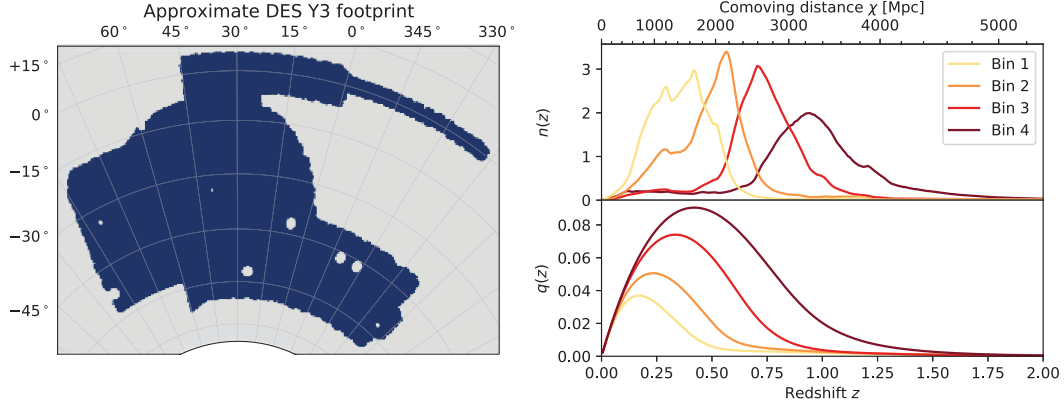
Figure 2. *Left*: DES Y3 survey footprint used in this work. *Right*: Normalized redshift distributions $n(z)$ from DES Y1 (top) and corresponding lensing efficiency functions $q(z)$ at the fiducial cosmology (bottom).

can write both C_ℓ and $\xi_\pm$ as integrals over $\ln k$. We show the corresponding (normalized) integrands in Fig. 1 for different values of ℓ and θ. Information from different physical k-modes in $P_{\rm NL}$ contribute to a given ℓ in C_ℓ, and since $\xi_\pm$ is a Fourier transform of C_ℓ, information in different k-modes get further redistributed into different θ scales.

2.2 Baseline model

Following Krause et al. (2017), we compute the non-linear power spectrum $P_{\rm NL}$ using the Boltzmann code CAMB (Lewis et al. 2000; Howlett et al. 2012) with the HALOFIT extension to non-linear scales (Smith et al. 2003) with updates from Takahashi et al. (2012). Later in Section 6.2, we investigate the effect of alternative prescription for the non-linear matter power spectrum from either an emulator (Lawrence et al. 2017) or the introduction of baryonic effects based on hydrodynamical simulations (Schaye et al. 2010). Consistent with the DES Y3 analysis, we vary six parameters of the ΛCDM model, namely the total matter density parameter $\Omega_{\rm m}$, the amplitude of structure σ_8, the baryon density parameter $\Omega_{\rm b}$, the Hubble parameter h (where $H_0 = 100\,h\,{\rm km\,s^{-1}\,Mpc^{-1}}$), the spectral index of the primordial curvature power spectrum $n_{\rm s}$ and the neutrino physical density parameter $\Omega_\nu h^2$. Throughout this paper we assume the Planck 2018 (Planck Collaboration et al. 2020) best-fit cosmology derived from TT,TE,EE+lowE+lensing+BAO data. The list of parameters, their definition, fiducial values used as inputs for simulations (see Section 4) and priors are shown in Table 1.

In addition, our baseline model includes a number of observational and astronomical systematic effects, parametrized by nuisance parameters that we marginalize over.

• *Shear calibration bias.* To account for uncertainties in shear calibration, we model the observed shear $\gamma^i_{\rm obs}$ in redshift bin i from the true shear γ^i by

$$\gamma^i_{\rm obs} = (1 + m_i)\gamma^i, \tag{4}$$

where m_i is the multiplicative shear bias, constant within each redshift bin i (Huterer et al. 2006; Heymans et al. 2006). These biases act as an overall rescaling for each redshift bin pair, such that

theoretical predictions are scaled as

$$C^{ij}_\ell \rightarrow (1 + m_i)(1 + m_j)C^{ij}_\ell, \tag{5}$$

$$\xi^{ij}_\pm(\theta) \rightarrow (1 + m_i)(1 + m_j)\xi^{ij}_\pm(\theta). \tag{6}$$

The posterior on these parameters is typically strongly dominated by the tight prior, a centered Gaussian of standard deviation 0.005 (see Table 1). Therefore, we approximate the posterior by marginalizing analytically over these nuisance parameters by a simple modification of the covariance matrix, as explained Section 2.3. This procedure allows us to reduce the parameter space and hence decrease the variance of importance sampling estimators (see Section 5). We use the same priors on m_i's for both statistics, but we do not require these multiplicative bias corrections to be strictly equal. In fact, they may slightly differ since biases are redshift dependent and contributions along the line of sight are mixed into angular scales differently.

• *Bias in the redshift distributions.* To account for uncertainty in the means of the redshift distributions, we model the estimated $n_{\rm obs}(z)$ to be shifted from the true $n(z)$. That is, we have

$$n^i_{\rm obs}(z) = n^i(z - \Delta z_i), \tag{7}$$

with a bias Δz_i for each redshift bin i.

• *Intrinsic alignment (IA).* The intrinsic shapes of galaxies are correlated through various mechanisms, such that the cosmic shear power spectrum receives contribution from the auto-correlation of intrinsic shapes, $C^{ij}_{\ell,{\rm II}}$, and the cross-correlation of intrinsic shapes with the shear field, $C^{ij}_{\ell,\gamma{\rm I}}$. For our baseline model, we use the so-called Non-Linear Alignment (NLA) model, proposed by Hirata & Seljak (2004); Bridle & King (2007), to compute $C^{ij}_{\ell,{\rm II}}$ and $C^{ij}_{\ell,\gamma{\rm I}}$, which is mathematically equivalent to replacing the lensing efficiency $q(\chi)$ in Eq. (1) in the following way

$$q^i(\chi) \rightarrow q^i(\chi) - A(z(\chi))n^i(\chi), \tag{8}$$

with

$$A(z) = -A_{\rm IA}\bar{C}_1\rho_c\frac{\Omega_{\rm m}}{D(z)}\left(\frac{1+z}{1+z_0}\right)^{\alpha_{\rm IA}}, \tag{9}$$

where $\rho_c = 3H_0^2/8\pi G$ is the critical density. Here $D(z)$ is the linear growth factor, $\bar{C}_1$ is a normalization constant set to $5 \times 10^{-14}\,M_\odot^{-1}\,h^{-2}\,{\rm Mpc}^3$ (Brown et al. 2002) and we set the pivot redshift at $z_0 = 0.62$ as done in Troxel et al. (2018a); Samuroff et al.

(2019). The amplitude $A_{\rm IA}$ and power-law scaling with redshift, $\alpha_{\rm IA}$, are treated as free parameters of the model with uniform priors over the range $[-5, +5]$ for both.

The full modeling pipeline described above is implemented in the software package CosmoSIS (Zuntz et al. 2015).

2.3 Covariance and likelihood

Both sets of point statistics, C_ℓ^{ij} and $\xi_\pm^{ij}$, measured from data at multipoles ℓ and angular separation θ, are stacked into two data vectors which are modeled as multivariate Gaussian variables with expected values described above by Eqs. (1) and (3). We use Gaussian analytic covariance matrices computed with CosmoSIS for all the cosmological inference in this work. The covariance for the power spectra C_ℓ can then be written as

$$\mathrm{Cov}\left(C_\ell^{ij}, C_{\ell'}^{i'j'}\right) \approx \delta_{\ell\ell'} \frac{D_\ell^{ii'} D_\ell^{jj'} + D_\ell^{ij'} D_\ell^{ji'}}{(2\ell+1)f_{\rm sky}} \qquad (10)$$

where i, j and i', j' denotes the redshift bin pairs associated with the two considered C_ℓ's, $D_\ell^{ij} \equiv C_\ell^{ij} + N_\ell^{ij}$ is the sum of the signal and noise power spectra, $\delta_{\ell\ell'}$ is the Kronecker delta function and $f_{\rm sky}$ is the fractional sky coverage set to $f_{\rm sky} = 0.1181$ in this work (corresponding to $4872\,\mathrm{deg}^2$, the approximate DES Y3 area when including small, isolated regions rejected in the Gold catalog as presented in Sevilla-Noarbe et al. 2020). The shape noise contribution N_ℓ^{ij} is zero for cross-correlation and $\sigma_{e,i}^2/\bar{n}_i$ for auto-correlations, where $\sigma_{e,i}$ is the standard deviation of the measured galaxy shapes and $\bar{n}_i$ is the effective mean density of galaxies per unit sky area in redshift bin i. In practice, we estimate power spectra $\hat{C}_L^{ij}$ averaged over band powers L defined by $\ell_{\rm min}^L \le \ell < \ell_{\rm max}^L$ and their covariance matrix is obtained by averaging Eq. (10) accordingly,

$$\mathrm{Cov}\left(C_L^{ij}, C_{L'}^{i'j'}\right) = \frac{1}{\Delta_L}\frac{1}{\Delta_{L'}} \sum_{\ell \in L} \sum_{\ell' \in L'} \mathrm{Cov}\left(C_\ell^{ij}, C_{\ell'}^{i'j'}\right), \qquad (11)$$

where $\Delta_L = \ell_{\rm max}^L - \ell_{\rm min}^L$ is the number of multipoles in band L.

The covariance for the correlation functions $\xi_\pm$ is essentially a Fourier transform of Eq. (10), and can be written as

$$\mathrm{Cov}\left(\xi_\pm^{ij}(\theta), \xi_\pm^{i'j'}(\theta')\right) \approx$$
$$\int \frac{\ell\,\mathrm{d}\ell}{2\pi} J_n(\ell\theta) \int \frac{\ell'\,\mathrm{d}\ell'}{2\pi} J_n(\ell'\theta') \,\mathrm{Cov}\left(C_\ell^{ij}, C_{\ell'}^{i'j'}\right), \qquad (12)$$

where spherical Bessel functions J_n are of order $n = 0$ ($n = 4$) for ξ_+ (ξ_-).

As mentioned in the previous section, we do not vary shear calibration biases in the cosmological analysis in order to reduce the dimension of the parameter space and thus improve the accuracy of importance sampling (see Section 5). However, we do account for the uncertainty due to those nuisance parameters by marginalizing analytically, following the procedure laid out in Bridle et al. (2002) and extended in Taylor & Kitching (2010). Assuming independent Gaussian priors, and to first order in the shear biases m_i, the marginalized likelihood remains Gaussian with a marginalized

covariance receiving an extra term[1]

$$\mathrm{Cov}\left(C_L^{ij}, C_{L'}^{i'j'}\right) \rightarrow \mathrm{Cov}\left(C_L^{ij}, C_{L'}^{i'j'}\right)$$
$$+ \sigma_m^2 C_L^{ij} C_{L'}^{i'j'}\left(\delta_{ii'} + \delta_{ij'} + \delta_{ji'} + \delta_{jj'}\right), \qquad (13)$$

where $\delta_{\alpha\beta}$ is the Kronecker symbol and $\sigma_m = 0.005$ is the standard deviation of the Gaussian prior on shear biases. The real-space covariance matrix is modified in exactly the same way, by replacing C_L's by $\xi_+(\theta)$ or $\xi_-(\theta)$.

We now comment on approximations made in the covariance matrix. First, we do not account for the survey geometry in either harmonic or real space as it has little impact for the DES Y3 footprint (Troxel et al. 2018b; Friedrich et al. 2020). Second, we note that the choice of Gaussian covariance (and Gaussian likelihood) is an approximation that matches the choice of Gaussian simulations. However, as shown in Barreira et al. (2018), the Gaussian covariance is largely sufficient even for non-Gaussian simulations. The next leading term is the so-called super-sample covariance term, accounting for correlations with k-modes larger than the survey footprint, but even this term is largely subdominant for a survey like DES Y3, as shown in Friedrich et al. (2020). This means that, for the purposes of this work targetted at DES Y3, we can safely employ Gaussian simulations and analyze them with a Gaussian covariance.

2.4 Contaminated data vectors: systematic effects and alternative modeling

The baseline model described above matches that in the DES Y1 analysis. However, there are known physical and instrumental effects that impact the measured C_ℓ and $\xi_\pm$ potentially differently, which may impact cosmological constraints depending on whether they affect scales that are used for the analysis. We therefore compute alternative theoretical data vectors, including one effect at a time, either modifying modeling or including additional biases in the data vectors from systematic effects.

- *Non-linear matter power spectrum.* Our fiducial model is based on the HALOFIT prescription (Takahashi et al. 2012) to model the impact of non-linear gravitational evolution of the large-scale structure at small scales, *i.e.* $k \gtrsim 0.2\,h\,\mathrm{Mpc}^{-1}$. However, it is known to be accurate only up to 5% for $k \le 5\,h\,\mathrm{Mpc}^{-1}$ and degrading for smaller scales. We recompute the fiducial data vectors using the matter power spectrum emulator from Lawrence et al. (2017), a Gaussian process interpolator based on the Mira-Titan Universe simulations (Heitmann et al. 2016), leaving the rest of the pipeline unchanged. With respect to HALOFIT, the emulator predicts a power spectrum roughly 5% lower in the range $0.2-2\,h\,\mathrm{Mpc}^{-1}$ with damped acoustic oscillation features. The cosmic shear power spectra and two-point functions are respectively reduced by about 5% at most for multipoles $\ell \sim 1000$ and angular separations $\theta \sim 10'$, which is about 10% (respectively 40%) of the error bars for the auto-correlation of redshift bin 1 (redshift bin 4) at these scales.

---

[1] This derivation starts from equation (24) in Taylor & Kitching (2010), noting that the prior covariance is diagonal with coefficients σ_m^2 and that the mean is $(1+m_i)(1+m_j)C_\ell^{ij}$. Taking derivatives of the mean with respect to m_k gives $(\delta_{ki} + \delta_{kj})C_\ell^{ij}$, to first order in m_k, and summing over indices k leads to Eq. (13). Note that this expression slightly differs from that found in Hildebrandt et al. (2017) as our parametrization is different (we allow all shear biases to vary independently).

Parameters	Symbols	Fiducial values	Priors	IS proposal distributions
Total matter density	$\Omega_{\rm m}$	0.3111	$\mathcal{U}(0.1, 0.6)$	Uniform in $(S_8, \sqrt{\Omega_{\rm m}})$, see Section 5.2.1.
Density fluctuation amplitude	σ_8	0.8076	$\mathcal{U}(0.5, 1.3)$	
Baryon density	$\Omega_{\rm b}$	0.04897	$\mathcal{U}(0.03, 0.12)$	$\mathcal{U}(0.03, 0.12)$
Hubble parameter	h	0.6766	$\mathcal{U}(0.55, 0.91)$	$\mathcal{U}(0.55, 0.91)$
Spectral index	$n_{\rm s}$	0.9665	$\mathcal{U}(0.87, 1.07)$	$\mathcal{U}(0.87, 1.07)$
Physical neutrino density	$\Omega_\nu h^2$	0.00083	$\mathcal{U}(0.0006, 0.01)$	$\mathcal{U}(0.0006, 0.01)$
Intrinsic alignment amplitude	$A_{\rm IA}$	0	$\mathcal{U}(-5, 5)$	$\mathcal{N}(0, 1.5)$
Intrinsic alignment redshift dependence	$\alpha_{\rm IA}$	0	$\mathcal{U}(-5, 5)$	$\mathcal{U}(-5, 5)$
Photo-z shift in bin i ($i = 1, 2, 3, 4$)	Δz_i	0	$\mathcal{N}(0, 0.005)$	$\mathcal{N}(0, 0.005)$
Shear bias in bin i ($i = 1, 2, 3, 4$)	m_i	0	$\mathcal{N}(0, 0.005)$	None (analytical marginalization)

Table 1. Cosmological and nuisance parameters in the baseline model. Uniform distributions in the range $[a, b]$ are denoted $\mathcal{U}(a, b)$ and Gaussian distributions with mean μ and standard deviation σ are denoted $\mathcal{N}(\mu, \sigma)$.

- *Baryonic feedback.* Baryonic processes within dark matter haloes redistribute matter and therefore impact the matter power spectrum at small scales. Energy injection from active galactic nuclei causes a small suppression of the matter power spectrum in the range $k \sim 1\text{–}10\,h\,{\rm Mpc}^{-1}$, and cooling as well as star formation enhance it at smaller scales (Chisari et al. 2018; Schneider et al. 2019). In order to model the impact of baryons on the fiducial data vectors, we rescale the non-linear matter power spectrum by the ratio of the matter power spectra measured in the OWLS simulations (van Daalen et al. 2011) with dark matter only, $P_{\rm DM}(k, z)$, and with AGN feedback, $P_{\rm AGN}(k, z)$, such that

$$P_{\rm NL}(k, z) \rightarrow P_{\rm NL}(k, z) \frac{P_{\rm AGN}(k, z)}{P_{\rm DM}(k, z)}, \tag{14}$$

as was done for the real space analysis of DES Y1, Troxel et al. (2018a). Note that we also derive scale cuts from this modified power spectrum in Section 3.

- *Intrinsic alignments from tidal torquing.* The NLA model accounts for tidal alignment (TA) mechanisms but not for tidal torquing (TT) ones that were proposed by Catelan et al. (2001); Crittenden et al. (2001); Mackey et al. (2002) as extra contributions in the observed shear power spectrum. These contributions were unified, including cross terms, into a single model (TATT) in Blazek et al. (2019), following a perturbation theory expansion of the tidal field. The TATT model was applied to DES Y1 data in Samuroff et al. (2019). Here, we adopt the same model and measure biases on data vectors including (part or all of) TA and TT contributions with respective amplitudes A_1 and A_2, and redshift dependence parametrized by power-law α_1 and α_2. We follow Samuroff et al. (2019) and fix the source bias to $b_g^{\rm src} = 1$, accounting for the density-tidal field term in the TA component (which is not included in the NLA model). Note that NLA is a special case of TATT with $A_2 = 0$ and $b_g^{\rm src} = 0$.

- *Point-spread function leakage.* The point-spread function (PSF) needs to be estimated and accounted for when measuring the ellipticities of galaxies. It is usually measured at the positions of stars and interpolated to the positions of galaxies, while modeling residuals can be estimated from a fraction of stars reserved for this purpose (Zuntz, Sheldon et al. 2018; Jarvis et al., 2016). PSF ellipticity residuals leak directly into cosmic shear measurements and may introduce biases. In particular, the PSF does not have the symmetries of gravitational lensing and has roughly equal E- and B-mode signals. We use the measurements from DES Y3 data presented in Jarvis et al. (2020) and a similar parametrization of the bias in the two-point functions $\xi_\pm(\theta)$ (although for simplicity we only keep the dominant term and fix $\beta = 1$), given by

$$\Delta\xi_\pm(\theta) = \rho_1^\pm(\theta) - \alpha\rho_2^\pm(\theta). \tag{15}$$

Here, $\rho_1^\pm$ is the auto-correlation function of PSF ellipticity residuals, $\rho_2^\pm$ is the cross-correlation between the model and residual ellipticities and α is the leakage coefficient. It is, however, difficult to directly evaluate the equivalent of $\rho_{1/2}$ in harmonic space directly because of the bias created by the noise power spectrum of the residuals (which is *not* a simple shape-noise). Instead, for the purpose of this work, we treat this bias as a small perturbation to the fiducial data vectors. Given the cross-covariance between $\xi_\pm$ and C_ℓ, we can compute the expectation value of the harmonic-space bias ΔC_ℓ conditioned on the real-space bias $\Delta\xi_\pm(\theta)$. More precisely, we combine Eq. (3) and Eq. (10) to compute an approximate, analytic Gaussian cross-covariance $\mathbf{C}_{\ell\pm} \equiv \text{Cov}\,(C_\ell, \xi_\pm(\theta))$ and the bias is estimated by

$$\left[\Delta C_\ell\right] = \mathbf{C}_{\ell\pm} \cdot \mathbf{C}_\pm^{-1} \cdot \left[\Delta\xi_\pm(\theta)\right], \tag{16}$$

where $\mathbf{C}_\pm$ is the covariance matrix of $\xi_\pm(\theta)$ given by Eq. (12). We used brackets to indicate data vectors and · for matrix-matrix and matrix-vector products. We find the biases induced by the PSF, ΔC_ℓ and $\Delta\xi_\pm(\theta)$, to be very small for DES Y3, in agreement with Jarvis et al. (2020), even for a leakage as high as 10% (*i.e.* $\alpha = 0.1$), which is excluded by measurements presented in Gatti, Sheldon et al. (2020).

- *Width of the redshift distributions.* In our fiducial pipeline, the uncertainty in the redshift distributions is solely encoded by a coherent shift, as shown in Eq. (7), capturing the principal mode of uncertainty. Here, we additionally probe the effect of underestimating the width of the redshift distribution. To do so, we convolve the redshift distribution with a Gaussian kernel of width $\sigma_z = 0.1$. Given that the widths of the redshift distributions are of order 0.2−0.3, this convolution increases the width by about 5−10%, consistent with typical width uncertainties found with self-organizing maps methods for DES Y3 (Buchs, Davis et al. 2019).

3   SCALE CUTS

As discussed in Section 1, the scale cuts imposed on the data vectors determine the physical k-modes of the cosmic shear field that are accessible through the two-point functions. In particular, since a hard cut in multipole space ℓ is not a hard cut in real space θ (and vice-versa), there is no straightforward translation between the two spaces, and a hard cut in k corresponds to neither. We explore below several methods to establish an approximate correspondence between scale cuts in harmonic and real space.

Methodologies employed for determining scale cuts in the literature are usually based on balancing the trade-off between systematic uncertainty and statistical uncertainty (Hildebrandt et al. 2017; Troxel et al. 2018a; Hikage et al. 2019). The scale cuts are

usually chosen to be such that the systematic uncertainty introduced by errors in the modeling are subdominant to the statistical uncertainty determined by the survey characteristics (*e.g.* area, density of galaxies). In particular, the modeling of intrinsic alignments (Krause et al. 2017; Samuroff et al. 2019) and the impact of baryons at small scales (Chisari et al. 2018; Schneider et al. 2019), both connected to small-scale, non-linear, astrophysical processes, typically drives small-scale cuts, while observational considerations, such as PSF residuals and shear calibration uncertainty, determine the large-scale cuts. For the real space analysis of DES Y1, Troxel et al. (2018a) chose small-scale cuts for each redshift bin such that differences between $\xi_\pm$ data vectors, with or without the effect of baryons, is less than 2%. The impact of baryons was modeled from the ratio of the matter power spectra measured in the OWLS simulations, as in Eq. (14). No additional scale cuts were applied for IA modeling uncertainties, given robustness tests presented in Krause et al. (2017). The DES Y1 scale cuts are listed in Table 2. We will present and discuss scale cuts used in HSC Y1 and KiDS-450 analyses in Section 6.3.

For this analysis, we fix the large-scale cut at $\theta_{max} = 10°$ and $\ell_{min} = \pi/\theta_{max} = 18$ (because signal-to-noise ratio is low in the largest-scale bin) and focus on different methods to derive the small-scale cuts. To derive the scale cuts we need to specify a number of quantities associated with the survey properties, such as the redshift distribution, the survey area and the number density of galaxies. We have chosen to use numbers that match the DES Y3 dataset. However, we note that the framework we developed here can be easily adapted for a different survey. As an illustrative exercise, we will present results in Section 6 that use all scales measured in the simulations described in Section 4. In order to maintain consistency between sections, we therefore include this option before presenting three realistic methods.

(i) *No scale cuts.* In Section 6, we will perform measurements using all available scales for which we have measurements.

(ii) $\ell \sim \pi/\theta$ *relation.* If cuts are available in one space, they can be very approximately translated to the other space using the relation $\ell \sim \pi/\theta$. In particular, we will use DES Y1 scale cuts in real space and approximately match them in harmonic space. To do so, we choose to use the geometric mean of the ξ_+ and ξ_- small-scale cuts, respectively θ^+_{min} and θ^-_{min}, *i.e.* we set $\ell_{max} = \pi/\sqrt{\theta^+_{min}\theta^-_{min}}$, which we find to preserve signal-to-noise ratio (as opposed to using either θ^+_{min} or θ^-_{min} to do the conversion). This is explained by the comparable marginal signal-to-noise ratios of ξ_+ and ξ_- measurements at their respective scale cuts.

(iii) *Physical mode cut-off* k_{max}. The next option we consider is motivated by Fig. 1. We pick a small-scale physical mode cut, k_{max}, and determine an effective corresponding ℓ_{max} and θ_{min} from $d \ln C_\ell/d \ln k$ and $d \ln \xi_\pm/d \ln k$. To do so, we write the power spectra C_ℓ and correlation functions $\xi_\pm(\theta)$ as integrals over wavenumber k, using the Limber formula and the change of variables $k = (\ell + 1/2)/\chi(z)$, and compute the corresponding scale $k_{>\alpha}$—which is a function of ℓ or θ—at which the integral reaches a fraction α of its total value, *i.e.*

$$\int_{-\infty}^{\ln k_{>\alpha}} d \ln k \left| \frac{d \ln X}{d \ln k} \right| = \alpha, \qquad (17)$$

where X is either C_ℓ, $\xi_+(\theta)$ or $\xi_-(\theta)$. Since ξ_+ receives negative contributions for a range of k-modes (especially at small scales), we consider the absolute value of the integrand to determine this
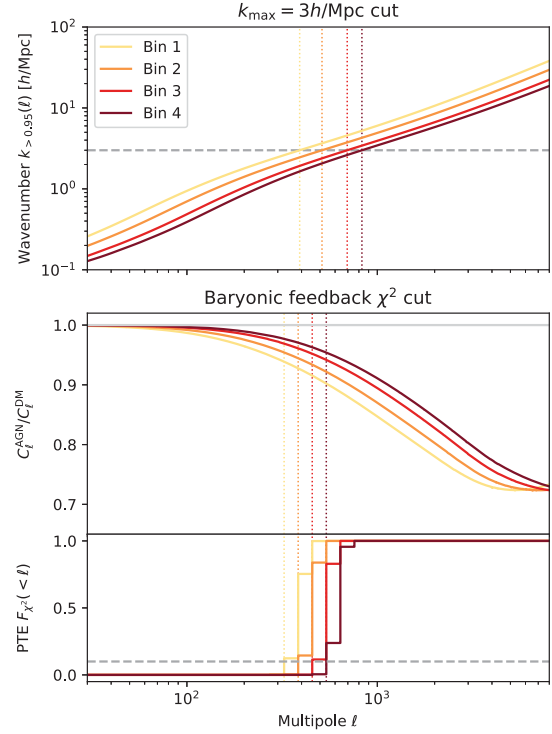

Figure 3. Harmonic space scale cuts derived from k_{max} and baryonic feedback cut-offs. In both plots, we show the curves corresponding to auto-correlations for bins 1 (yellow) through 4 (red) and derived ℓ_{max} cuts as the vertical dotted lines. We do not show cross-correlations for readability, although we apply the same method to derive cuts for those bins, which we report in Table 2. *Top:* Scale cuts derived from physical mode cut-off at $k_{max} = 3\,h\,\mathrm{Mpc}^{-1}$ (grey dashed line). For a given multipole ℓ, we compute the k-mode at which the Limber integral, Eq. (1), reaches 95% of its total value, $k_{>0.95}(\ell)$. We exclude multipoles with $k_{>0.95}(\ell) > k_{max}$, *i.e.* those that receive more than 5% of their signal from scales beyond k_{max}. *Bottom:* Scale cuts derived from baryonic feedback (from OWLS). The top panel shows the ratio of predicted C_ℓ with and without baryonic feedback. The bottom panel shows the probability-to-exceed $F_{\chi^2}(> \ell)$ of the χ^2 statistics computed between C_ℓ data vectors computed with baryonic feedback to that without (for the binning used in Gaussian simulations, see Section 4) when including all multipole bins below ℓ. We exclude multipoles with a χ^2 above its tenth percentile (grey dashed line).

cut[2]. We then compute the value ℓ_{max} (respectively θ_{min}) for which $k_{>\alpha}(\ell_{max}) = k_{max}$ (respectively $k_{>\alpha}(\theta_{min}) = k_{max}$). Here, we use a fraction of $\alpha = 0.95$, *i.e.* we keep scales for which 95% of the signal comes from modes under k_{max}. In other words, theoretical uncertainties beyond k_{max} may only affect 5% of the smallest scales included in the analysis. We will vary k_{max} from 1 to $5\,h\,\mathrm{Mpc}^{-1}$, which is the scale above which errors in the HALOFIT model exceed 10% (Takahashi et al. 2012). The results are shown in Fig. 3 for harmonic space and in Fig. 4 for real space, for $k_{max} = 3\,h\,\mathrm{Mpc}^{-1}$, which we use as our fiducial value, in the middle of the range $1–5\,h\,\mathrm{Mpc}^{-1}$.

(iv) *Impact of baryons.* Following the DES Y1 method, we

---

[2] We tested both with and without the absolute value, and found that including it yielded cuts with closer signal-to-noise ratio between harmonic and real spaces.
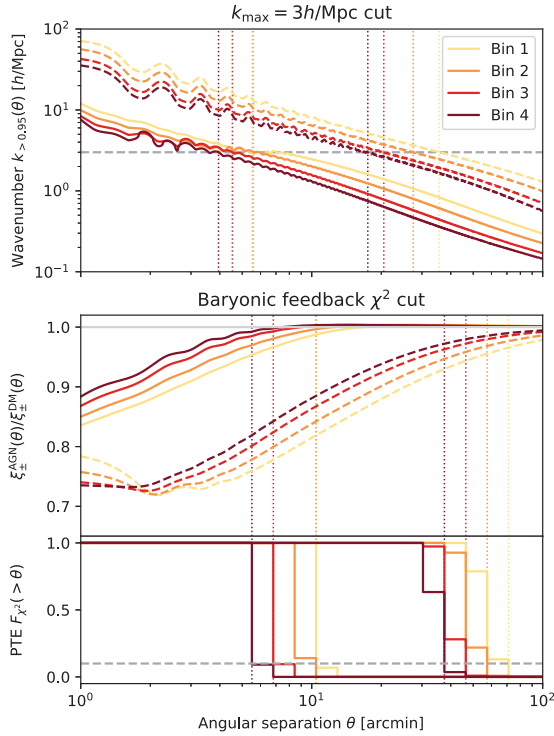
Figure 4. Real space scale cuts derived from $k_{\max}$ and baryonic feedback cut-offs, similar to Fig. 3 for real-space two-point functions $\xi_\pm(\theta)$. We use solid (respectively dashed) curves for ξ_+ (respectively ξ_-). The wiggles in $k_{>0.95}(\theta)$ are due to acoustic features and sign flipping of $d \ln \xi_\pm/d \ln k$ visible in Fig. 1. The bottom panel in the bottom plot should be read from large scales (right) to small scales (left), as it shows the probability-to-exceed of the χ^2 statistic, $F_{\chi^2}(> \theta)$ computed for bins with a separation angle above θ.

use baryonic feedback models to compare two-point data vectors with and without modeling baryons (using the same OWLS AGN model). The DES Y1 analysis set a fixed threshold for the fractional difference between the data vector with and without baryons. This threshold is, however, somewhat arbitrary. We improve on the method by instead requiring the χ^2 distance between the two data vectors, which incorporates correlations between elements of the data vectors, not to exceed the percentile corresponding to a fixed probability-to-exceed (PTE). We use a covariance matrix without shape-noise to preserve the theoretical motivation for the cut, alleviating the dependence on survey depth (except for the area through the $f_{\rm sky}$ factor). Given a binning scheme (see Section 4), we compute, separately for each redshift bin pair, χ^2 distances between data vectors, starting from the largest-scale bin and progressively including smaller-scale bins. At each step, we then compute the corresponding PTE for a χ^2 distribution with a number of degrees of freedom equal to the number of aggregated bins, denoted $F_{\chi^2}(< \ell)$. We set a threshold at the tenth percentile, *i.e.* we discard small-scale bins where $F_{\chi^2}(< \ell) > 0.1$. We plot $F_{\chi^2}(< \ell)$ in the lowest panel of Fig. 3 as a piecewise constant function matching bin edges. The procedure works similarly in real space, where we instead compute $\chi^2(\theta)$ and $F_{\chi^2}(> \theta)$, discarding small-angle bins θ where $F_{\chi^2}(> \theta) > 0.1$. This procedure allows us to obtain theoretically motivated cuts in both spaces with relatively little dependence on the threshold choice, as shown by the sharp transition in the lower

panels of Figs. 3 and 4. Note that this method is applicable to any kind of comparison between a fiducial and contaminated model.

We list all scale cuts used in the analysis (results presented in Fig. 9 and thereafter) in Table 2 and plot them in Figs. 5 and 6 for comparison.

4 SIMULATIONS

Simulations are essential in this work as they allow us to realistically capture the correlated information that is used by the harmonic and real space statistics, and by representing the survey geometry, galaxy density and noise level expected in the real survey. In particular, simulations allow us to generate pairs of C_ℓ and $\xi_\pm$ data vectors with the correct cross-covariance, which is challenging to compute analytically with good accuracy, especially when accounting for survey geometry.

Our fiducial analysis is targeted towards the DES Y3 cosmic shear analysis, which motivates the choice of tomographic redshift bins, redshift distributions, number density and shape noise. At the time of completing this analysis the DES Y3 shear catalog and redshift distribution were not finalized. As a result we only approximately match final DES Y3 choices. We use four tomographic redshift bins with redshift distributions taken from the DES Y1 dataset, as shown in Fig. 2. The number density for each redshift bin is fixed to $\bar{n} = 1.5$ gal/arcmin^2, with shape noise of $\sigma_e = 0.3$ per component in the fiducial analysis, and $\sigma_e = 0.3/\sqrt{2}$ for the *low noise* analysis (see Section 6.1). We use an approximate DES Y3 footprint, also shown in Fig. 2, with a survey area of 4872 deg^2. We note that the main conclusions of this study should be robust even though these numbers do not match exactly that in DES Y3.

We provide here a brief description of our simulations. Starting from fiducial power spectra C_ℓ^{ij} for redshift bins i and j, we generate a full-sky realization of the four correlated shear fields in HEALPix[3] (Górski et al. 2005) maps of resolution $N_{\rm side} = 4096$ (with an approximate resolution of 0.86′). To do so, we first generate the harmonic coefficients of the E-mode of the shear fields, $E_{\ell m}^i$, for multipoles up to $\ell_{\max} = 3N_{\rm side} - 1$. These coefficients are Gaussian random variables with covariance $\langle E_{\ell m}^i E_{\ell'm'}^j \rangle = \delta_{\ell\ell'}\delta_{mm'} C_\ell^{ij}/2w_\ell^2$, where we have included the HEALPix pixel window function w_ℓ. These variables are independent for different ℓ and m indices, such that they can be sampled in parallel. At fixed ℓ, m, the Cholesky decomposition of the covariance matrix (indexed by i, j) is used to generate $E_{\ell m}^i$ coefficients from four standard random variables, following a standard procedure to sample multivariate Gaussian variables. We then use the alm2map function of HEALPY (Zonca et al. 2019) in polarization mode, with $T_{\ell m}^i = B_{\ell m}^i = 0$, to generate the four correlated, true shear maps. Then, we draw random positions of galaxies within the DES Y3 footprint[4] in each redshift bin with density $\bar{n}$ and compute the values γ_i of the shear field at the positions of the galaxies[5] (indexed by i here). We then draw random intrinsic ellipticities of the galaxies $\mathbf{e}_i$ from a zero-mean normal

---

[3] http://healpix.sf.net
[4] Galaxies are drawn independently, therefore there is no clustering of source galaxies, which may cause B-mode patterns, beyond the scope of this paper. We also do not account for blending here, supposedly included in the shear biases.
[5] The shear field is thus sampled at fixed effective redshift and not at the redshift of the galaxies.

Scale cut	Fiducial S/N	$C_\ell/\xi_\pm$ cut	Redshift bin pairs									
			1-1	1-2	1-3	1-4	2-2	2-3	2-4	3-3	3-4	4-4
No scale cut	69.8 (C_ℓ)	ℓ_{max}	8192	8192	8192	8192	8192	8192	8192	8192	8192	8192
	62.8 ($\xi_\pm$)	θ_{min}^+	1.0′	1.0′	1.0′	1.0′	1.0′	1.0′	1.0′	1.0′	1.0′	1.0′
		θ_{min}^-	10.0′	10.0′	10.0′	10.0′	10.0′	10.0′	10.0′	10.0′	10.0′	10.0′
DES Y1 ($\ell \sim \pi/\theta$)	54.8 (C_ℓ)	ℓ_{max}	423	474	532	532	670	670	752	844	844	947
	43.8 ($\xi_\pm$)	θ_{min}^+	7.2′	7.2′	5.7′	5.7′	4.5′	4.5′	4.5′	3.6′	3.6′	3.6′
		θ_{min}^-	90.6′	72.0′	72.0′	72.0′	57.2′	57.2′	45.4′	45.4′	45.4′	36.1′
$k_{max} = 3\,h\,{\rm Mpc}^{-1}$	53.0 (C_ℓ)	ℓ_{max}	391	441	491	513	512	586	619	694	751	830
	50.1 ($\xi_\pm$)	θ_{min}^+	5.5′	5.0′	6.0′	6.0′	5.6′	5.1′	5.0′	4.5′	4.1′	3.9′
		θ_{min}^-	35.8′	31.6′	28.5′	27.1′	27.1′	24.0′	22.9′	20.5′	18.6′	17.5′
Baryonic feedback χ^2	47.5 (C_ℓ)	ℓ_{max}	341	364	410	429	397	432	456	485	507	532
	40.3 ($\xi_\pm$)	θ_{min}^+	11.5′	11.4′	10.5′	9.3′	10.0′	9.2′	9.0′	7.6′	7.4′	6.1′
		θ_{min}^-	67.7′	62.3′	57.7′	51.3′	58.6′	50.9′	49.6′	48.3′	43.4′	40.9′

Table 2. Small-scale cuts used in this work (in particular the results shown in Fig. 9) and the signal-to-noise ratio S/N computed from the the fiducial data vector. The large-scale cuts are $\ell_{min} = 18$ and $\theta_{max}^\pm = \pi/\ell_{min} = 600' = 10°$ for all bins.

distribution with variance σ_e^2 and finally compute the observed ellipticity, given by

$$\mathbf{e}_i^{obs} = \frac{\gamma_i + \mathbf{e}_i}{1 + \gamma_i^* \mathbf{e}_i}. \tag{18}$$

The next step is to compute the two-point data vectors from these mock catalogs both in harmonic and real space. In harmonic space, we use a pseudo-C_ℓ estimator computed with NaMaster (Alonso et al. 2019). To do so, we first compute ellipticity maps, for both components, by averaging ellipticities in each pixel. We use the count map as the inverse-variance weighting mask. We use NaMaster to measure mask-deconvolved, binned power spectra $\hat{C}_\ell^{ij}$ in 36 logarithmically spaced bins between $\ell_{min} = 18$ and $\ell_{max} = 2N_{side} = 8192$. The measurements are corrected for the pixel window function introduced above (by multiplying raw C_ℓ by w_ℓ^2) and we correct for the noise power spectrum bias in each bin by applying random rotations to ellipticities and subtracting the mean power spectrum of 16 realizations to the measured auto power spectra. In real space, we use the package TreeCorr (Jarvis et al. 2004) to estimate $\xi_\pm$ from the mock catalogs in 30 log-spaced bins between $\theta_{min} = 1'$ and $\theta_{max} = 600'$. For both harmonic and real space measurements, the large-scale cut corresponds to 10°, which is of the order of the largest scale that can be measured well in the DES footprint, and the small-scale cut corresponds to the resolution of the simulations.

Figures 5 and 6 show two-point data vectors measured from the 500 simulations we use for the analysis. The input C_ℓ power spectra are recovered well within 5% of the error bars at all considered scales[6]. Corresponding real-space two-point functions are recovered within 5% and 10%, respectively, for ξ_+ and ξ_-, for scales larger than 10′, which is accurate enough for our purposes. At scales below 10′, resolution effects of at most 20% of the error bars for ξ_+ are visible and a simple correction is applied (see below). For ξ_-, these effects are larger, leading us to discard these scales for ξ_-, although these are already cut off in all scale cuts we consider. We therefore apply an additive correction to each simulation corresponding to the difference between the fiducial data vector and the mean measured data vector to correct for small resolution and

binning effects, which we approximate to be realization independent. This allows us to use the fiducial data vector as a reference point while not changing the variance of measured data vectors. We verified that the shifts in cosmological parameters arising from this difference are indeed negligible, thus validating *a posteriori* the simulations and this correction.

5   FAST DERIVATION OF MEAN POSTERIOR POINT USING IMPORTANCE SAMPLING

For a given choice of scale cuts, we wish to measure the difference in the posterior of cosmological parameters, for each simulations presented in the previous section, between harmonic and real space two-point statistics measurements. Running two full Markov Chain Monte Carlo (MCMC) analyses for each simulation and each choice of scale cuts is computationally unfeasible. As a result, we employ importance sampling (IS) in this work to rapidly compute, for each simulation, a point estimator of S_8 in both harmonic and real space, which we denote $\widehat{S_8}|_{C_\ell}$ and $\widehat{S_8}|_{\xi_\pm}$ (or simply $\widehat{S_8}$ to mention both). We choose to use *the mean of the posterior* as point estimator, as it is less noisy than the mode of the posterior (or maximum a posteriori) when evaluated from a fixed sample. Since the likelihood is Gaussian, we can generate a library of theoretical data vectors (for C_ℓ and $\xi_\pm$) for a sample of cosmological parameters representative of the full prior space, and use them to rapidly compute importance weights for all simulations and scale cuts. The IS pipeline and its validation are detailed in the following subsections. We show the distributions of $\widehat{S_8}$ computed from simulations in Fig. 8 and compare it to the posteriors derived from a single (noiseless) fiducial data vector without scale cuts. While expectedly close, these distributions are not mathematically equal, *i.e.* the spread of $\widehat{S_8}$ does not necessarily trace the width of the posterior. Moreover, $\widehat{S_8}|_{C_\ell}$ and $\widehat{S_8}|_{\xi_\pm}$ are correlated variables—the two-dimensional distribution of which we will study in Section 6, see *e.g.* Fig. 9.

5.1   Improved weighted importance sampling

We now provide a brief introduction to the theory of importance sampling. Given a sample of size n of parameters $\{\theta_i\}_{1 \le i \le n}$ from a proposal distribution with density q, one can estimate the expectation value of a function $\langle f(\theta) \rangle_p$ under a target distribution with

---

[6] Note that the sampling noise creates a small bias at very large multipoles $\ell \gtrsim 4000$, likely due to the choice of resolution parameter $N_{side} = 4096$ with our fiducial galaxy density, leading to many empty pixels.

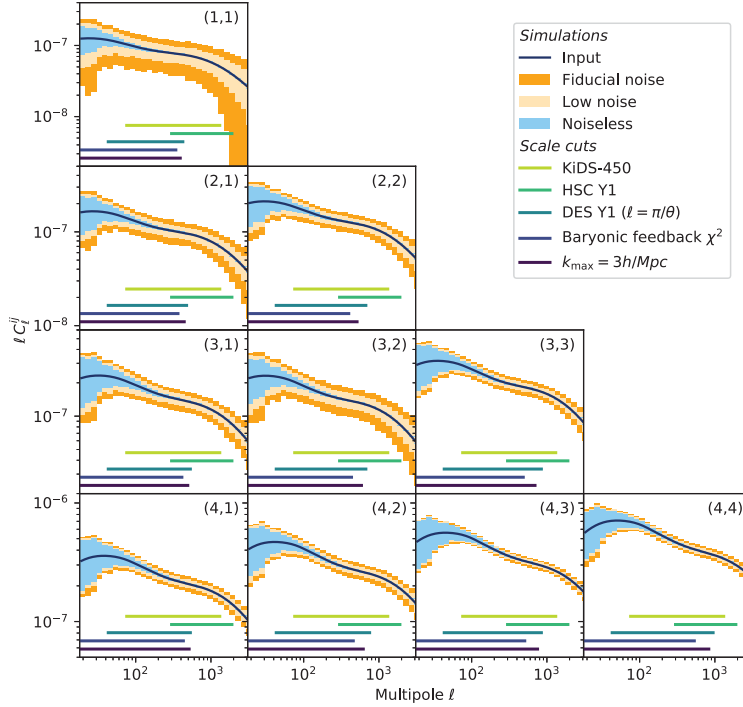**Figure 5.** Power spectra C_ℓ measured from Gaussian simulations described in Section 4 and scale cuts used in the analysis in Section 6. The input power spectrum are plotted in dark blue. Boxes show the measured mean and standard deviation in each ℓ bin, in orange for the fiducial noise level ($\sigma_e = 0.3$), in moccasin for the low noise level ($\sigma_e = 0.3/\sqrt{2}$) and in light blue for the noiseless case (where each galaxy shape corresponds to the shear field value). The ranges of scale cuts used in the analysis are shown as solid horizontal lines.

density p with the estimator

$$\hat{f}_n = \frac{1}{n} \sum_{1 \leq i \leq n} w_i f(\theta_i), \tag{19}$$

where $w_i \equiv p(\theta_i)/q(\theta_i)$ are ratios of the densities, called importance weights. For our study, the target distribution is the posterior $p(\theta) \propto \mathcal{L}(X|\theta)\,\pi(\theta)$, where X is either C_ℓ or $\xi_\pm$ measured from simulations, $\mathcal{L}$ is the likelihood and π is the prior. However, the posterior, computed this way, has unknown normalization. Therefore, one needs to normalize the importance weights such that they sum to 1 and then use the weighted average estimator instead of the standard estimator Eq. (19). This operation introduces an order $O(1/n)$ bias which can be reduced to $O(1/n^2)$ by using the improved weighted importance sampling (IWIS) estimator from Skare et al. (2003), where weights are modified to $w_i' = w_i/S_{-i}$ with $S_{-i} = \sum_{j \neq i} w_j$ and then normalized, providing final IS weights $\tilde{w}_i = w_i'/\sum_{1 \leq i \leq n} w_i'$.

The efficiency of importance sampling strongly depends on the choice of proposal distribution q, *i.e.* how the parameter sample is generated. The effective number of samples is given by $N_{\mathrm{eff}}^{\mathrm{IS}} = 1/\sum_{1 \leq i \leq n} \tilde{w}_i^2$. It is bounded by the total number of samples n, corresponding to the case where the proposal distribution is equal to the target distribution and all weights are equal to $1/n$. In practice, the closer the proposal distribution q is to the target distribution p, the higher the effective number of samples will be, and therefore the more accurate the IWIS estimator is.

5.2 Cosmological parameter sampling

For the purposes of this work, the proposal distribution q of cosmological parameters needs to efficiently cover all regions in parameter space where the posteriors corresponding to each simulations have support. We detail the choice of proposal distribution in the next section, motivated by posteriors obtained with MCMC from few random realizations of the data vectors.

5.2.1 Choice of proposal distribution

We choose to sample all parameters independently, except for σ_8 and Ω_m. Therefore, the proposal distribution can be factorized into the product of distributions for (σ_8, Ω_m) and all the other parameters. We adopt a uniform distribution in the (σ_8, Ω_m)-plane within a band along the degeneracy observed in weak lensing experiments, which better constrain the combination $S_8 \propto \sigma_8 \sqrt{\Omega_m}$. To do so, we note that the Jacobian of the transformation $(\sigma_8, \Omega_m) \rightarrow (S_8, \sqrt{\Omega_m})$ is constant, such that we can uniformly sample over a rectangle in the $(S_8, \sqrt{\Omega_m})$-plane in order to obtain the desired distribution. We draw S_8 in the range $[0.7, 0.9]$ and $\sqrt{\Omega_m}$ within $[\sqrt{0.1}, \sqrt{0.6}]$ (*i.e.* the prior range of Ω_m). We sample over other cosmological parameters (Ω_b, h, n_s and $\Omega_\nu h^2$) uniformly within their prior bounds specified in Table 1. For intrinsic alignment parameters, we opt for a uniform distribution for the intrinsic alignment tilt parameter α_{IA}; however, we sample the amplitude of intrinsic alignments A_{IA} with a Gaussian proposal distribution of standard deviation 1.5 and centered at zero, as the prior range is much broader than observed posterior distributions. Finally, we adopt the Gaussian priors over
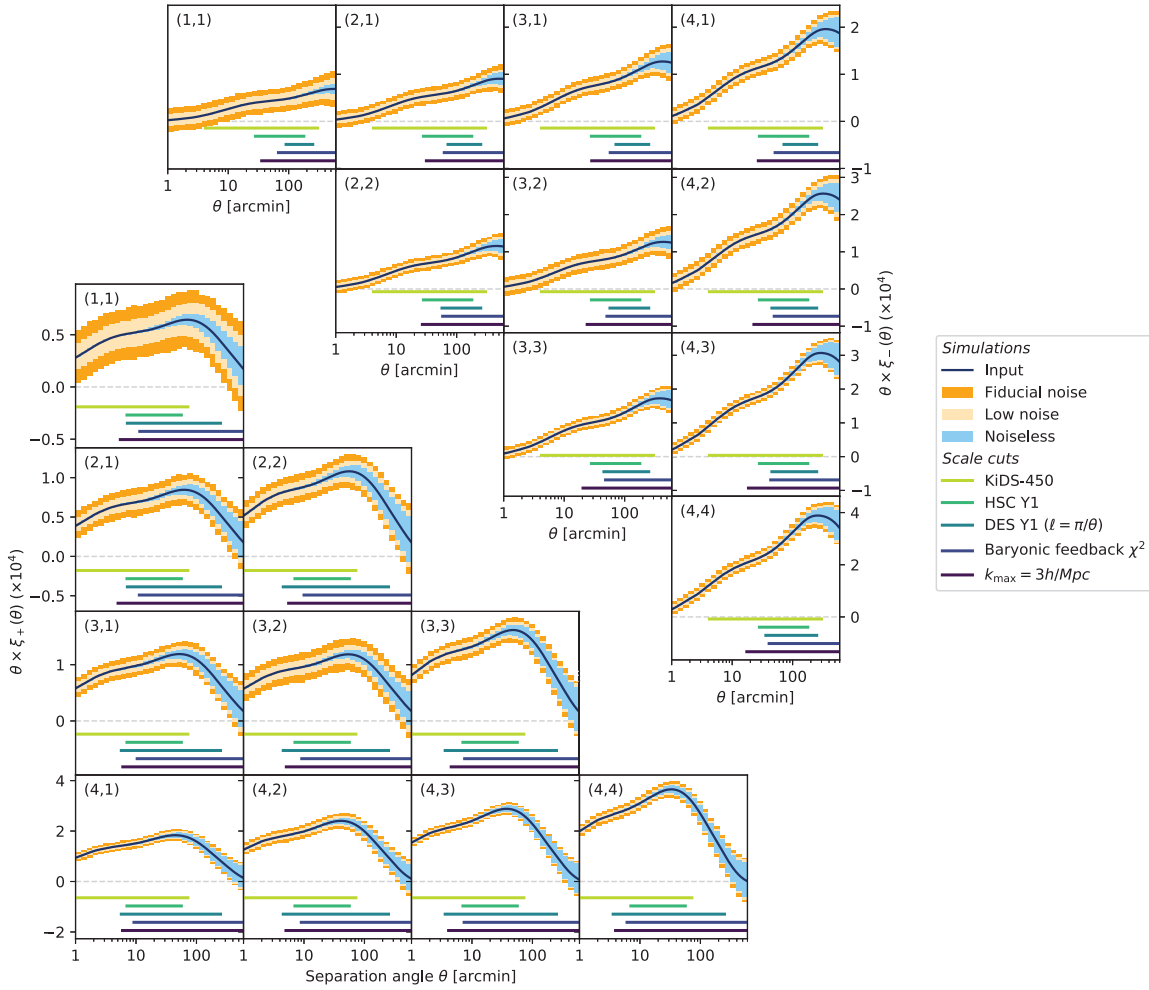
Figure 6. Two-point functions $\xi_{\pm}(\theta)$ measured from Gaussian simulations described in Section 4 and scale cuts used in the analysis in Section 6, similar to Fig. 5. The input two-point functions are plotted in dark blue. Boxes show the measured mean and standard deviation in each θ bin, in orange for the fiducial noise level ($\sigma_e = 0.3$), in moccasin for the low noise level ($\sigma_e = 0.3/\sqrt{2}$) and in light blue for the noiseless case (where each galaxy shape corresponds to the shear field value). The ranges of scale cuts used in the analysis are shown as solid horizontal lines.

redshift biases Δz_i's for the proposal distribution. As explained in Section 2.3, we dot not sample shear biases as they are marginalized analytically. Given these choices, summarized in the fourth column of Table 1, the proposal distribution is therefore proportional to the product of redshift bias priors and the proposal distribution of $A_{\rm IA}$, the other marginal distributions being uniform within their support.

5.2.2 Sample generation

In order to generate a sample with good space-filling properties, we use optimized Latin Hypercube Sampling (LHS). More precisely, we first generate 10^6 samples within the unit hypercube $[0, 1]^{12}$ with standard LHS and then optimize its design using the Enhanced Stochastic Evolutionary algorithm[7] (Jin et al. 2005). This tech-

nique operates by exchanging coordinates of points to make the sample closer to uniform (which is formally quantified by a *discrepancy criterion*). This reduces the variance of the IS estimator while maintaining its convergence properties and leaving it unbiased (see Packham 2015, for a derivation). Finally, we apply to the LHS sample the inverse cumulative distribution function of the proposal distribution q to generate the sample of cosmological parameters.

5.3 Fast derivation of posterior mean

For each simulation, indexed j, from which we obtained a measurement X_j (where X is either C_ℓ or $\xi_{\pm}$), we compute the IWIS estimator of the mean under the posterior given by

$$\widehat{\theta}_j = \frac{1}{n} \sum_{1 \leq i \leq n} \tilde{w}_{ij} \theta_i, \tag{20}$$

---

[7] We use the implementation from the Surrogate Modeling Toolbox python library (Bouhlel et al. 2019), available at `https://smt.readthedocs.io/en/latest/_src_docs/sampling_methods/lhs.html`.
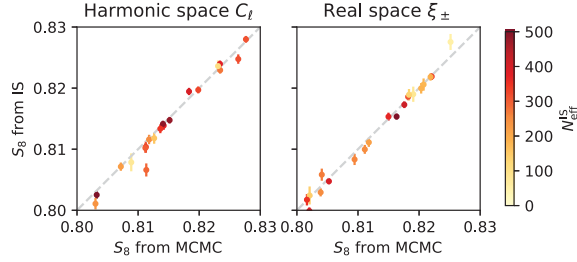
Figure 7. Validation of the importance sampling (IS) pipeline by comparison of estimated mean S_8 obtained with standard nested sampling of the posterior (horizontal axis) and with importance sampling (vertical axis) for 20 noisy data vectors. The error bars show the error on the IS estimator, which depends on the effective number of samples, shown by the color of the error bars. This test uses no scale cuts: applying scale cuts increases the effective number of samples and further reduces errors.

where the normalized weights $\tilde{w}_{ij}$ are computed as explained in Section 5.1 from unnormalized weights, given by

$$w_{ij} = \frac{\mathcal{L}(X_j|\theta_i)\pi(\theta_i)}{q(\theta_i)}. \qquad (21)$$

This computation can be accelerated and parralelized by noting that

$$\log w_{ij} = -\frac{1}{2}\left\|\mathbf{L}X_j - \mathbf{L}X(\theta_i)\right\|^2 + \log\pi(\theta_i) - \log q(\theta_i) + c, \qquad (22)$$

up to an irrelevant constant c, where $\mathbf{L}$ is the Cholesky decomposition of the covariance matrix, $\mathbf{C} = \mathbf{L}^\intercal\mathbf{L}$. We first compute $\mathbf{L}X_j$ and $\mathbf{L}X(\theta_i)$ for all j and i (slow but parallelizable operations), and then we compute the first term for all pairs i and j (fast operations). The computation thus becomes linear in the number of samples plus the number of simulations—instead of the product—and we can analyze all 500 simulations in under a minute on a single 28-core node.

To validate the importance sampling pipeline and the choice of proposal distribution, we draw 20 noisy data vector realizations in harmonic and real space (uncorrelated), which were obtained by independently sampling the likelihoods at the fiducial model. We then run a standard nested sampling analysis with MultiNest (Feroz et al. 2009) and compare the mean of the parameter posteriors obtained from the nested sampling to those obtained with importance sampling. Figure 7 shows the comparisom in the case where we use all the measured scales described in Section 4, which represents the most stringent test. In the plot, the points are colored by their effective number of samples. We obtain biases well below 0.5% for most realizations as seen in Fig. 7, with effective number of samples typically in the few hundreds. Note that for all other cuts, we obtain much higher effective number of samples, typically few thousands for $k_{\max} = 5\,h\,\mathrm{Mpc}^{-1}$ to order 10^4 for $k_{\max} = 1\,h\,\mathrm{Mpc}^{-1}$, making errors on the posterior means negligible for our purposes.

As a complementary test, we also compare the full shape of the marginalized posterior derived from nested sampling and importance sampling, shown in Fig. 8 for the fiducial, noiseless data vector, in both spaces and without scale cuts. In this case, the importance sampling pipeline recovers the mean with an accuracy of 0.1% and the width within 10%, with very similar results in harmonic and real space. For comparison, we also show the distribution of mean posterior points evaluated from simulations (orange histograms).
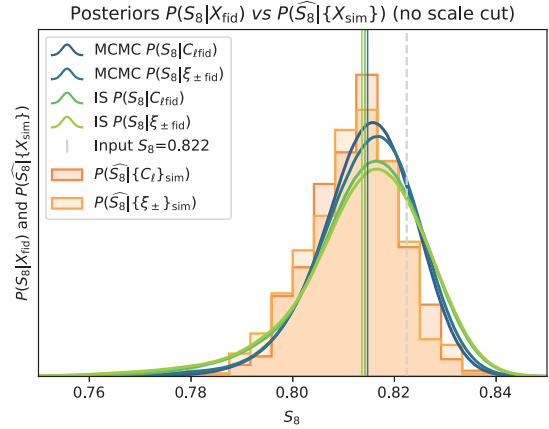

Figure 8. Comparison of marginal posterior distributions on S_8 on the fiducial data vectors $P(S_8|X_{\mathrm{fid}})$ in harmonic ($X = C_\ell$) and real space ($X = \xi_\pm$) without scale cuts, derived from standard MCMC sampling (blue) and IS (green). Colored vertical lines (mostly overlapping) indicate the mean under each posterior and the black vertical line shows the input S_8 value. In orange, we show the histogram of mean posterior points $\widehat{S_8}$ derived from C_ℓ and $\xi_\pm$ measurements for 500 simulations, see Section 6. The gray dashed line show the input S_8 value.

6   RESULTS

This section presents our main results. In Section 6.1, we probe the joint distribution of S_8 estimators, $\widehat{S_8}|_{C_\ell}$ and $\widehat{S_8}|_{\xi_\pm}$, derived from measurements of two-points statistics in harmonic and real space, on 500 simulated mock DES Y3 surveys, for different scale cuts. In particular, we measure the Pearson correlation coefficients of these estimators and the scatter of their difference to gauge the expected consistency of harmonic and real space analyses. In Section 6.2, we compute the biases $\Delta\widehat{S_8} = \widehat{S_8}|_{\xi_\pm} - \widehat{S_8}|_{C_\ell}$ due to various potential theoretical, astrophysical and observational residual systematic uncertainties and compare it with the scatter measured from statistical fluctuations, $\sigma(\Delta\widehat{S_8})$. Finally, we apply scale cuts from published analyses of HSC and KiDS-450 data and discuss observed discrepancies in S_8 in Section 6.3. Although we partially focus our analysis on S_8, we also report results on σ_8 and Ω_{m}, with figures in Appendix A.

Before describing our results, we draw attention to important features of the marginalized S_8 posterior. As can be seen in Fig. 8, it is slightly asymmetric towards lower values, and both the mode and the mean are biased low, with respect to the input S_8 value, on a fiducial data vector. This *projection effect* is expected when a high-dimensional posterior, with its associated degeneracies and prior boundaries, is projected onto one dimension. Similar trends were observed with other cosmic shear analyses (*e.g.*, Joachimi et al. 2020). As a consequence, our measurements of posterior means generally appear to be biased low with respect to the input S_8 parameter (similarly, σ_8 is biased low and Ω_{m} high). However, this problem pertains to the choice of point estimate—*e.g.*, the mode, median, or, like here, the mean of the marginal posterior—and we find similar trends in both harmonic and real space. Moreover, the truth value consistently lies within the $\sim 1\sigma$ interval of the posterior. Therefore, this apparent bias does not interfere with the question of the consistency between analyses, as long as we relate to the mean of the posterior evaluated from the fiducial data vector as a reference point, and shifts thereof.
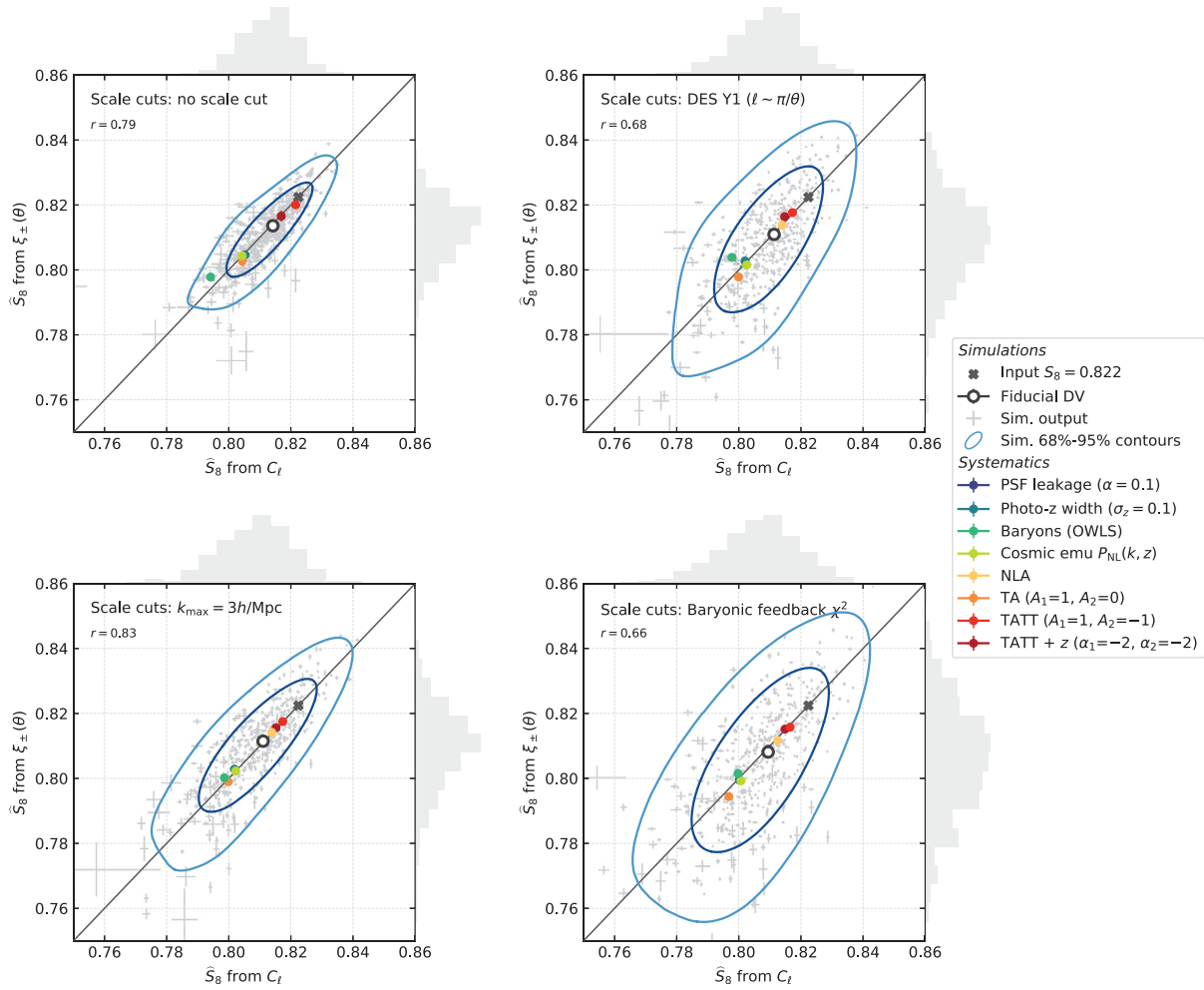
Figure 9. Distribution of estimated $\widehat{S_8}$ from real space (vertical axis) *vs* harmonic space (horizontal axis) analyses, and biases induces by unmodeled systematic effects. Each plot corresponds to a different scale cut indicated in the upper left. The scattered gray points show the mean of the posteriors of the Gaussian simulations described in Section 4 in both real and harmonic space, as well as the error associated with the IS estimator (mostly indistinguishable for realistic scale cuts). Note these error bars denote the uncertainty on the mean of the posteriors rather than their width. Blue contours show the 68% and 95% contours of these points. Their Pearson correlation coefficient r is reported in the upper left. Marginal distributions are shown by the gray (unnormalized) histograms above and to the right of each panel. The mean of the posterior for the fiducial, noiseless data vector is shown by the white dot encircled in black. Data vectors contaminated with various unmodeled systematic effects are analyzed in the same way and results are shown by the colored points. The value of S_8 used as input is shown by the cross. The result of the analysis of the fiducial data vector provides a reference point for the estimator, which is expected to differ from the input due to projection effects (while remaining consistent in terms of the width of the posterior).

6.1 Estimated parameter differences between harmonic and real space cosmic shear

We now apply the importance sampling methodology described in Section 5 to compute the mean posterior points $\widehat{S_8}|_{C_\ell}$ and $\widehat{S_8}|_{\xi_\pm}$ for each simulation using harmonic and real-space measurements described in Section 4, for different scale cuts described in Section 3.

We consider four fiducial scale cuts: (i) no scale cuts, *i.e.* using all measured scales from the simulations ($\ell_{max} = 8192$, $\theta^+_{min} = 1'$ and $\theta^-_{min} = 10'$) (ii) using DES Y1 real-space cuts converted to harmonic space with the relation $\ell = \pi/\theta$, (iii) a k_{max} type cut with a threshold at $3\,h\,\mathrm{Mpc}^{-1}$, and (iv) cuts derived from baryonic feedback contamination. The baryonic feedback cut is the most conservative choice, while the k_{max} cut is (relatively) more aggressive,

and the DES Y1 ($\ell = \pi/\theta$) lies in between (see Figs. 5 and 6). Results are shown in Fig. 9, where we show with gray error bars the mean of the posterior for each simulation, and in blue the 68% and 95% contours of the distribution sampled by these points. Note that these contours do not necessarily reflect the width of the posteriors themselves, but rather how much posteriors may shift for multiple realizations of the cosmic shear measurements at fixed cosmology. We quantify the statistical discrepancy between harmonic and real-space cosmic shear analyses by characterizing the distribution of the difference between mean posterior points, $\sigma(\Delta\widehat{S_8})$, derived from harmonic and real-space measurements. We show histograms of $\Delta\widehat{S_8}$ in Fig. 10, for the four sets of scale cuts used above (as well as HSC Y1 and KiDS-450 scale cuts, discussed in Section 6.3). We measure its standard deviation as well as the Pearson correlation

coefficients, r, between $\widehat{S_8}|_{C_\ell}$ and $\widehat{S_8}|_{\xi_\pm}$, which are reported in Table 3. If the mean posterior shifts from individual statistics have the same spread ($\sigma(\widehat{S_8}|_X)$ for $X = C_\ell, \xi_\pm$, also reported for reference), the two metrics measure the same quantity, but when the constraints change, the correlation coefficient r is likely a better measure of the common information used in the two statistics. The spread, however, is useful to determine how likely a certain observed difference between parameters measured by the two statistics is, *i.e.* an observed difference larger than this number would be indicative of a tension between the two analyses. We proceed similarly for Ω_m and σ_8, see Figs. A1 and A2.

Quantitatively, we find that, using all scales available in simulations, the standard deviation of $\widehat{S_8}|_{C_\ell}$ and $\widehat{S_8}|_{\xi_\pm}$, $\sigma(\widehat{S_8}|_X)$ is 0.010 for both statistics ($X = C_\ell, \xi_\pm$). The spread of the difference is $\sigma(\Delta\widehat{S_8}) = 0.007$, for the fiducial noise level and DES Y3-like survey characteristics. These are lower bound on the error that can be reached with DES Y3 data. For realistic scale cuts, we find that $\sigma(\widehat{S_8}|_X)$ increases similarly for both statistics while $\sigma(\Delta\widehat{S_8})$ varies significantly across scale cuts (by a factor of almost 2), as seen in Figs. 9 and 10. We find significantly smaller variations for $\sigma(\Delta\widehat{\Omega_m})$ and $\sigma(\Delta\widehat{\sigma_8})$. In particular, we observe that the k_{max} cut provides the highest correlation coefficient at about 83%, with similar spread in either space. For this cut, we find $\sigma(\widehat{S_8}|_{C_\ell}) \equiv \sigma(\widehat{S_8}|_{\xi_\pm}) = 0.013$ and $\sigma(\widehat{S_8}|_{C_\ell} - \widehat{S_8}|_{\xi_\pm}) = 0.0076$. For the DES Y1 ($\ell \sim \pi/\theta$) cut, which by comparison of θ_{min} is close to a k_{max} cut between 2 and $3\,h\,\mathrm{Mpc}^{-1}$, we find a lower correlation coefficient of 68%, indicating that the simplistic conversion fails at capturing the same information in each estimator. Moreover, posterior means are slightly more scattered in real space, consistent with the fact that, for these scale cuts, the fiducial signal-to-noise ratio is lower in real space (see Table 2). Similarly, the baryonic feedback cut that we have applied here yields asymmetric results with a tail for lower values in real space, as expected from the difference in predicted signal-to-noise ratio (47 for C_ℓ and 40 for $\xi_\pm$), and a correlation coefficient of 68%. Overall, we measure $\sigma(\Delta\widehat{S_8})$ to be a fraction $\sim 0.6-0.9$ of the scatter for individual statistics, which is to be compared to $\sqrt{2} \approx 1.4$ for fully uncorrelated estimators. For σ_8 and Ω_m, we observe a similar trend for the scatter of the difference to increase for stricter cuts. However, the correlation coefficients r are much less sensitive to scale cuts, which we interpret as a consequence of the strong, banana-shaped degeneracy between σ_8 and Ω_m visible for all scale cuts—the difference in posterior means between statistics is subdominant to the variance of posterior means across realizations.

We proceed to further explore the distribution of parameters shifts and attempt to gain insight into the generalization of our results to the next generation of weak lensing surveys. We perform two tests, one where we repeat measurements for k_{max}-type cuts for different values of k_{max} in the range $1-5\,h\,\mathrm{Mpc}^{-1}$, which is an indication of the confidence in small-scale modeling, and one where we emulate a deeper survey by reducing shape-noise. In Fig. 11, we plot the 68% contours obtained when varying k_{max} from 5 down to $1\,h\,\mathrm{Mpc}^{-1}$. We first observe that these cuts return very similar constraints in both spaces, indicating that, they are well-performing and physically motivated choices, if consistency is desired. We find that $\sigma(\widehat{S_8}|_{C_\ell} - \widehat{S_8}|_{\xi_\pm})$ goes from 0.0049 to 0.019, with a correlation coefficient going from 89% to 56%, as expected when decreasing k_{max} from 5 to $1\,h\,\mathrm{Mpc}^{-1}$. We find that the posterior mean derived from the fiducial data vectors shifts towards lower values for decreasing k_{max}, albeit with negligible differential biases. In Fig. 12, we show 68% contours obtained when decreasing the noise level, which here we achieve by dividing the variance of intrinsic ellipticities σ_e^2 by two (while keeping the

density fixed) in simulations. Contours shrink, as expected, towards the input value. Both the spread of the posterior means and the spread of the difference decrease, though we note that the amount to which they decrease with respect to one another depends on the choice of scale cut, making it difficult to separate the effect of noise and scale cuts on discrepancies in the harmonic and real space analyses. In other words, shape-noise acts as an effective cut-off at small scales where it dominates the signal.

We expect that numerical results presented here will not change dramatically for the real DES Y3 data. At the time of conducting this work, the DES Y3 catalogs and pipeline were not yet finalized, but the number density, footprint and redshift distributions we used do capture the essential properties of the final DES Y3 data.

6.2 Bias from systematic effects

We now compute posterior shifts due to theoretical and astrophysical uncertainties. As argued in the introduction, different effects may impact C_ℓ and $\xi_\pm$ measurements differently, resulting in non-equal shifts in posterior distributions, thus creating a *differential* bias. Although it is difficult to assess all potential biases and their interplay, we nonetheless propose to measure individual (differential) biases from a selection of systematics, representative of theoretical and observational uncertainties pertaining to the current generation of weak lensing surveys. To do so, we apply the IS analysis pipeline to noiseless theory data vectors computed with varying modeling assumptions, or contaminated with spurious signals, as detailed in Section 2.4. Results are overlaid in Figs. 9 and 10 for comparison with expected shifts from statistical fluctuations described in the previous section. In particular, we show the result of analyzing the following data vectors (we indicate in italic the label used in the plots):

- *Fiducial DV*. Noiseless data vector computed from the baseline model detailed in Section 2 with the fiducial cosmology (see Table 1).
- *PSF leakage $\alpha = 0.1$*. Data vector computed from the fiducial data vector with an additive bias measured from PSF ellipticities and residuals, with a leakage fraction $\alpha = 0.1$.
- *Photo-z width ($\sigma_z = 0.10$)*. Noiseless data vector computed at the fiducial cosmology but with redshift distributions convolved by a Gaussian kernel of width $\sigma_z = 0.1$.
- *Baryons (OWLS)*. Noiseless data vector computed at the fiducial cosmology with a power spectrum including small-scale rescaling due to baryonic feedback, see Eq. (14).
- *Cosmic emu $P_{NL}(k, z)$*. Noiseless data vector computed with a non-linear matter power spectrum modelled with the Mira-Titan emulator, as opposed to the HALOFIT prescription.
- *NLA*. Noiseless data vector computed from the baseline model at the fiducial cosmology, but with a non-zero amplitude ($A_{IA} = 1.5$) of the intrinsic alignments (IA), assuming the fiducial NLA model. This is a check that the cosmology is not significantly affected by intrinsic alignments when the model is correct. We note that the small shifts with respect to the fiducial data vector indicate that projection effects—that shift the posterior mean from input parameter values—are somewhat dependent on the input parameters.
- *TA ($A_1 = 1$, $A_2 = 0$)*. Noiseless data vector computed at the fiducial cosmology but where we switched the IA model to TATT. For this first TATT data vector, we only include the TA component, which includes the additional density-tidal field contribution, with respect to NLA. Current constraints on TATT amplitudes $A_{1,2}$ and redshift-dependence parameters $\alpha_{1,2}$ remain fairly weak. However,
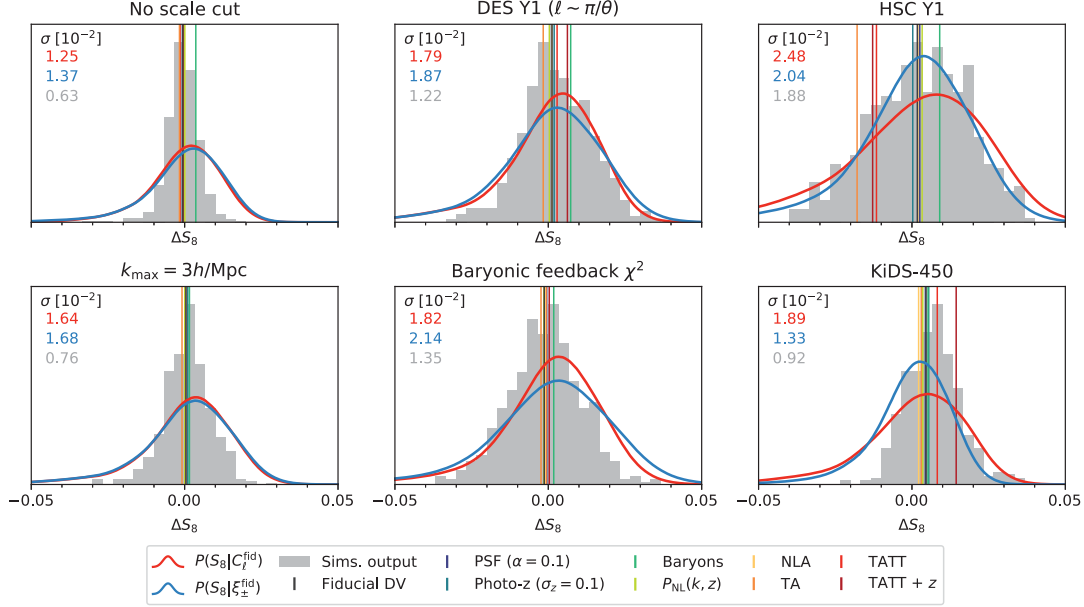
Figure 10. Distribution of differential biases $\widehat{\Delta S_8} \equiv \widehat{S_8}|_{\xi_\pm} - \widehat{S_8}|_{C_\ell}$ between real space and harmonic space analyses. The histograms show the posterior mean difference derived from simulations. They are compared to individual posteriors, $P(S_8|X)$ with $X = C_\ell, \xi_\pm$, derived from fiducial data vectors and shifted with respect to their own mean S_8. Each panel corresponds to a different scale cut used in this analysis, as indicated above. The standard deviations (multiplied by 100) of the C_ℓ posterior (red), $\xi_\pm$ posterior (blue) and $\widehat{\Delta S_8}$ histograms (gray) are reported in the upper left of each panel. Vertical lines indicate the differential biases computed for data vectors contaminated with unmodeled systematics.

		Statistics					
Parameter (θ)	Scale cut	$\sigma\left(\theta\,\middle|\,C_\ell^{\text{fid}}\right)$	$\sigma\left(\theta\,\middle|\,\xi_\pm^{\text{fid}}\right)$	$\sigma\left(\widehat{\theta}\,\middle|_{C_\ell}\right)$	$\sigma\left(\widehat{\theta}\,\middle|_{\xi_\pm}\right)$	$\sigma\left(\Delta\widehat{\theta}\right)$	Pearson r
S_8	(i) No scale cut	0.013	0.014	0.010	0.010	0.006	0.79
	(ii) DES Y1 ($\ell \sim \pi/\theta$)	0.016	0.019	0.012	0.014	0.011	0.68
	(iii) $k_{\max} = 3\,h\,\text{Mpc}^{-1}$	0.016	0.017	0.013	0.013	0.008	0.83
	(iv) Baryonic feedback χ^2	0.018	0.021	0.014	0.018	0.014	0.66
σ_8	(i) No scale cut	0.058	0.060	0.050	0.047	0.031	0.79
	(ii) DES Y1 ($\ell \sim \pi/\theta$)	0.070	0.070	0.056	0.053	0.041	0.71
	(iii) $k_{\max} = 3\,h\,\text{Mpc}^{-1}$	0.071	0.064	0.057	0.052	0.036	0.79
	(iv) Baryonic feedback χ^2	0.077	0.077	0.063	0.061	0.046	0.73
Ω_m	(i) No scale cut	0.049	0.054	0.042	0.043	0.026	0.81
	(ii) DES Y1 ($\ell \sim \pi/\theta$)	0.063	0.063	0.049	0.046	0.033	0.76
	(iii) $k_{\max} = 3\,h\,\text{Mpc}^{-1}$	0.063	0.059	0.050	0.046	0.029	0.82
	(iv) Baryonic feedback χ^2	0.069	0.068	0.053	0.050	0.034	0.78

Table 3. Comparison of the scatter of parameter estimators between harmonic and real space two-point statistics. For each parameter $\theta = S_8, \sigma_8, \Omega_m$ and two-point statistics $X = C_\ell, \xi_\pm$, we report the scatter of the mean of the posterior $\sigma(\widehat{\theta}|_X)$ compared to the width of the posterior for the fiducial data vector $\sigma(\theta|X^{\text{fid}})$ for power spectra and correlation functions, the scatter of the difference of posterior means between the two statistics $\sigma(\Delta\widehat{\theta})$ (*penultimate column*) and the Pearson correlation coefficient r of posterior means (*last column*). If $\widehat{\theta}|_{C_\ell}$ and $\widehat{\theta}|_{\xi_\pm}$ were independent random variable with equal variance, we would have $\sigma(\Delta\widehat{\theta}) = \sqrt{2}\,\sigma(\widehat{\theta}|_X)$.

Samuroff et al. (2019) showed that all four parameters are of order unity and that DES Y1 data favor $A_1 > 0$, $A_2 < 0$ and show a mild preference for $\alpha_{1,2} < 0$. We therefore use $A_1 = 1$ and $A_2 = 0$ here, and no redshift dependence, *i.e.* $\alpha_{1,2} = 0$.

- *TATT* ($A_1 = 1$, $A_2 = -1$). Noiseless data vector computed at the fiducial cosmology with the TATT model, incorporating the TT contribution with $A_1 = 1$ and $A_2 = -1$, and no redshift dependence, *i.e.* $\alpha_{1,2} = 0$.

- *TATT + z* ($\alpha_1 = -2$, $\alpha_2 = -2$). Noiseless data vector computed

at the fiducial cosmology with the TATT model with both TA and TT contributions and redshift dependence with parameters $\alpha_{1,2} = -2$.

Biases should be compared with the mean posterior point from the analysis of the fiducial data vector ("Fiducial DV") and differences between harmonic and real space should be measured perpendicular to the gray diagonal (and, strictly speaking, multiplied by $\sqrt{2}$). For the three fiducial scale cuts, and given our DES Y3-like setup, we find most systematics tested here yield estimate S_8 well within 68% contours in the $(\widehat{S_8}|_{C_\ell}, \widehat{S_8}|_{\xi_\pm})$ plane and that the differences between harmonic and real space biases are typically
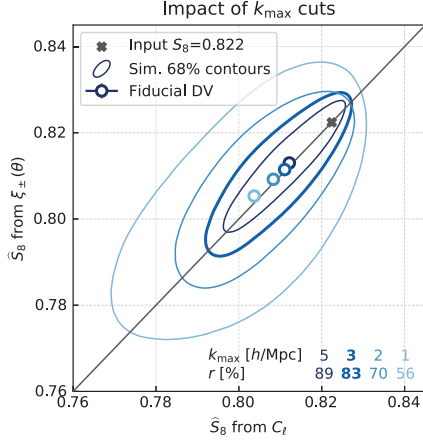
Figure 11. Impact of the k_{max} cut on the distribution of $\widehat{S_8}$. We show the 68% contours, similar to the lower left panel of Fig. 9, for k_{max} scale cuts, varying k_{max} from 1 to $5\,h\,\mathrm{Mpc}^{-1}$ (light to dark blue). The values of $\widehat{S_8}$ derived from the fiducial data vector are shown by the white dots encircled in blue.
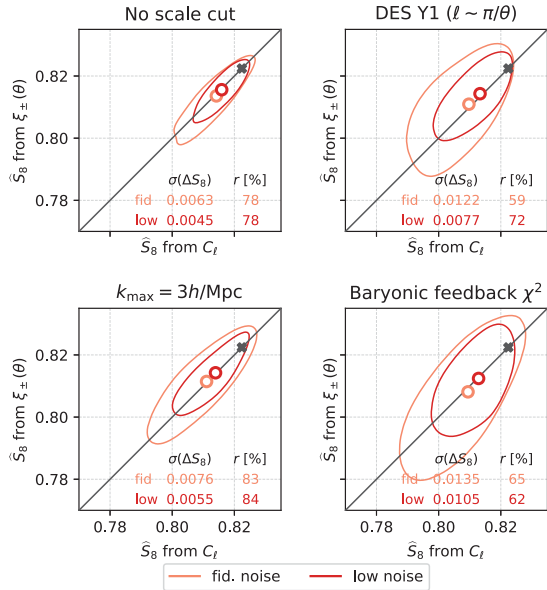

Figure 12. Impact of shape noise on the distribution of $\widehat{S_8}$. The low noise contours are obtained by dividing the variance of intrinsic ellipticities σ_e^2 by two in the simulations, which is, with respect to the covariance matrix, equivalent to a deeper survey with doubled galaxy density (see also Figs. 5 and 6). The values of $\widehat{S_8}$ derived from the fiducial data vector are shown by the white dots encircled in red.

within $\sim 0.5\sigma(\Delta\widehat{S_8})$, displaced along the diagonal. The largest bias comes from baryonic feedback, which lies beyond the 68% contour when no scale cuts are applied and approaches it for the "DES ($\ell \sim \pi/\theta$) cut. Then, smaller biases are found for the TA model and non-linear power spectrum and, to a lesser extent, data vectors contaminated with photo-z width—all of which result in biases of about 0.01 for each estimator, but generally negligible differential biases. When comparing TA and TATT models, we find, somewhat counter-intuitively, that the model including TT contributions yield

a smaller bias, on both statistics, than the TA-only model. This depends on details of how the NLA model is able to mimic TA and TT contributions and absorb the non-cosmological shear signal. However, we note that the choice of a negative A_2 reduces the overall IA contamination, especially on small scales, and that the TT part is likely canceling part of the beyond NLA contributions in TA. We conclude that the various effects we examined impact the two statistics similarly for the three fiducial scale cuts we show and do not bias one over the other for a DES Y3-like configuration. This indicates that these scale cuts capture sufficiently similar information for those systematics to have basically the same effect on both two-point statistics, with regard to S_8 estimation. For σ_8 and Ω_m (see Figs. A1 and A2), baryons do create a differential bias when no cut is applied, but are well controlled with realistic cuts. On the other hand, intrinsic alignments including TA and TT contributions, in particular with redshift dependence, create a mild differential bias, pushing σ_8 high and Ω_m low for harmonic space compared to real space. A possible explanation is that the redshift dependence, once the shear field is projected, becomes a scale-dependent effect which impacts both statistics differently. The contamination from PSF leakage and NLA (which is included in the model) are found to be negligible for all cuts.

In Fig. 11, we vary the k_{max} cut and find that, for most systematics, decreasing k_{max} does not create significant differential biases. We observe that $\widehat{S_8}$ moves similarly for the fiducial data vector and for most contaminated data vectors, although these are not shown to maintain readiblity. These shifts are therefore likely due to the lesser information content at $k_{max} = 1\,h\,\mathrm{Mpc}^{-1}$, combined with projection effects. When decreasing shape-noise in Fig. 12, we see two countereffects: with lower noise, the posterior tightens closer to the true input value, but the reweighting of small scales increases some biases—particularly baryons and IA— beyond the tightened 68% contours for the most aggressive cuts.

We note that, by testing effects one at a time, we cannot probe all their combinations and how they add up to increase biases, or reversely, cancel each other out. Finally, we point out that for all systematic effects tested here, the IS pipeline provides accurate estimates, characterized by effective numbers of samples in the range $10^3 - 10^4$. We ran standard MCMC chains for a limited number of cases and found excellent good agreement for all of them.

6.3 Comparison with previous work

The HSC (Hamana et al. 2020; Hikage et al. 2019) and KiDS (Hildebrandt et al. 2017; Köhlinger et al. 2017) collaborations have published cosmic shear analyses in both harmonic and real spaces using, respectively, HSC Year 1 and KiDS-450 data, sharing shear catalogues and redshift distributions across analyses, and found discrepancies in their cosmological constraints of order $0.5 - 1\sigma$. We now repeat the exercise of analyzing simulations and contaminated data vectors using corresponding scale cuts found in those publications, that is, removing bins outside the corresponding $\theta_{min}/\theta_{max}$ and ℓ_{min}/ℓ_{max} ranges while maintaining the binning we used throughout this work. We caution the reader that here we use the same simulations of a DES Y3-like survey as presented in previous sections, and only apply published scale cuts for comparison with cuts shown above. Since the simulations do not capture the depth and geometry of the different surveys, we cannot directly apply the conclusions here to the published KiDS and HSC results. We can, however, gain qualitative insights to how the chosen scale cuts might have resulted
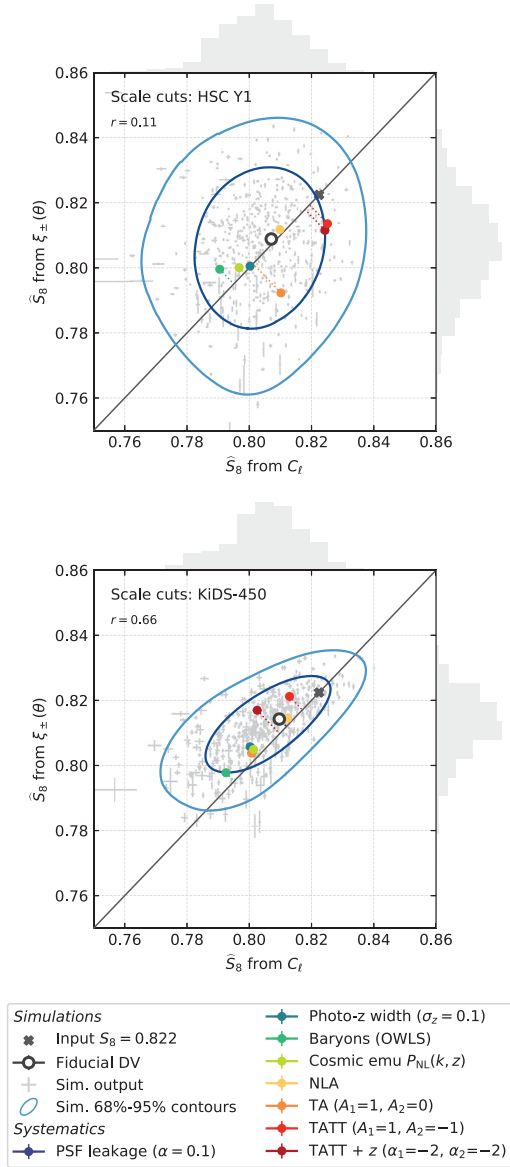
B-modes at lower multipoles from PSF leakage. The small-scale cut $\ell_{max} = 1900$ is chosen to avoid uncertainties from intrinsic alignments at scale smaller than $1-2\,h^{-1}$ Mpc, corresponding to $\ell \gtrsim 2000$. Both analyses share modeling choices, *e.g.* for the non-linear matter power spectrum, intrinsic alignments and the impact of baryons. Although the fiducial model assumes no baryonic feedback, the authors test the analytic model of Harnois-Déraps et al. (2015) and find that constraints shift by less than $1\,\sigma$.

For the KiDS-450 analyses, scale cuts are also chosen to be identical across redshift bins. In real space (Hildebrandt et al. 2017), a large scale cut of $72'$ is imposed on ξ_+ because of additive shear biases at larger scales, while ξ_- is used up to $300'$, only limited by the extent of the KiDS-450 patches. Small scale cuts of $0.5'$ and $4.2'$ are applied to ξ_+ and ξ_- due to uncertainties in the model and low signal-to-noise ratio. In harmonic space (Köhlinger et al. 2017), the large scale cut is $\ell_{min} = 76$, limited by the extent of KiDS-450 patches, and the small-scale cut of $\ell_{max} = 1310$ is chosen to be in the regime where the quadratic power spectrum estimator is found to recover simulation inputs. We note that authors caution that the real-space analysis uses more non-linear scales information, therefore expecting differences.

In the four aforementioned HSC and KiDS-450 papers, the robustness of the results with respect to model choices were thoroughly explored, in particular the impact of baryonic feedback and intrinsic alignment, as well as to instrumental effects (some of which dictated scale cuts, as mentioned above). In particular, KiDS-450 analyses, which use small-scale measurements, include baryonic effects in their baseline model. Both collaborations also model intrinsic alignments with the NLA model in each analysis.

Figure 13 shows the distribution of $\widehat{S_8}|_{C_\ell}$ and $\widehat{S_8}|_{\xi_\pm}$ and the impact of systematics when using HSC and KiDS-450 published scale cuts on a DES Y3-like survey. We present corresponding results for σ_8 and Ω_m in Figs. A1 and A2, respectively. For HSC scale cuts, we find that the correlation coefficient is of order 10% for S_8, σ_8 and Ω_m, somewhat consistent with findings in Section 6.7 and Appendix 5 of Hamana et al. (2020) obtained from running the full pipeline on one hundred N-body mock survey simulations (S_8 was found to show a correlation of 50%, albeit on the posterior median rather than the mean, though the difference may also arise from survey configurations). Noticeably, all systematic effects we probed point in the direction where σ_8 as measured from harmonic space is higher than σ_8 from real space measurements (and lower Ω_m), which coincides with actual observations, although the amplitudes are found to be smaller here than actual discrepancies observed in data, meaning that no single systematic may explain this discrepancy. It is possible that all systematic effects combined could create a more significant bias between the two analyses, though this would require further investigation. However, we also note that baryonic feedback points to a higher S_8 from real space measurement—matching observations in directions, but not in amplitude—while intrinsic alignments point in the other direction. Therefore, while we observe significant systematic trends in σ_8 and Ω_m, we also find that distribution of $\widehat{\Delta S_8}$ is significantly broader here than for other cuts, as shown in the top right panel of Fig. 10, and we refrain from attributing the observed difference in S_8 to either systematics or statistics. For KiDS-450 scale cuts, we observe a significant trend for real space measurement to yield higher mean of S_8 than harmonic space measurements, the former being typically closer to the input value in our simulations. This is likely due to a combination of the different scale cuts and projection effects. We find a higher correlation coefficient of 66% in this case, and note that all systematics have higher S_8 for real space measurements. In particular, we

Figure 13. Distribution and biases of $\widehat{S_8}$ from real (vertical axis) *vs* harmonic (horizontal axis) space for mock DES Y3 surveys analyzed with scale cuts that were used in the published cosmic shear analyses of HSC Y1 data (top, Hamana et al. 2020; Hikage et al. 2019) and KiDS-450 (bottom, Hildebrandt et al. 2017; Köhlinger et al. 2017). See Fig. 9 for a description of elements in the plot.

in the apparent large scatter between the constraints from real- and harmonic-space statistics.

For the analysis of HSC first-year data in real space (Hamana et al. 2020), scale cuts are the same for all redshift bin pairs. The small-scale cut is chosen so that the difference in $\xi_\pm$ from baryons (AGN model from Harnois-Déraps et al. 2015) is smaller than 5%. The large-scale cut is chosen from PSF contamination and impacts only ξ_+. They are $7.08' < \theta < 56.2'$ and $28.2' < \theta < 178'$ for ξ_+ and ξ_-, respectively. For the harmonic space analysis (Hikage et al. 2019), the cuts are also the same for all redshift bin pairs. The large-scale cut $\ell_{min} = 300$ is determined by the detection of

find that the bias created by intrinsic alignments from tidal torquing, especially with redshift dependence (and, for HSC, the TA model), lie close to the boundary of the 68% region in the $(\widehat{S_8}|_{C_\ell}, \widehat{S_8}|_{\xi_\pm})$ plane. While these observations are not sufficient to make any conclusive claim regarding observed discrepancies (*i.e.* distinguish a statistical fluke from systematic biases), they do shed some light on the interactions between the choice of scale cuts and systematic effects. Moreover, in the case of HSC, we note that a change in area increases error bars in the same proportion at all scales (through the $f_{\rm sky}$ coefficient in the covariance matrix, see Eq. (10)) and we find that our results still hold when using our "low noise" simulations: biases remain practically unchanged while $(\widehat{S_8}|_{C_\ell}, \widehat{S_8}|_{\xi_\pm})$ contours shrink, making those biases all the more concerning. A caveat is that to generate those simulations, we decrease the shape-noise $\sigma_e^2/\bar{n}$ by dividing the ellipticity standard deviation σ_e by 2, while HSC would be better matched by increasing the galaxy density $\bar{n}$, though the two should be equivalent with respect to shape-noise alone.

7 CONCLUSION

In this work, we have investigated the impact of scale cuts and systematic effects on the cosmological constraints derived from the analysis of cosmic shear two-point statistics in harmonic *vs* real space. As a quantity projected along the line-of-sight, the observed angular two-point statistic at a given scale receives contribution from a broad range of three-dimensional, Fourier k-modes, where physics is naturally described. Moreover, these contributions do not align perfectly between the harmonic and real space statistics, which are related through a Bessel integral. Therefore, imposing a hard cut in one space means imposing soft, or oscillatory, cuts in other spaces, making it difficult to find unambiguous correspondence between various analyses. In addition, theoretical uncertainties and observational systematic effects may induce differential biases that need to be disentangled from statistical fluctuations.

Motivated by discrepancies found in the literature on the parameter S_8 by the HSC Y1 (Hamana et al. 2020; Hikage et al. 2019) and KiDS-450 (Hildebrandt et al. 2017; Köhlinger et al. 2017) collaborations between their analyses of two-point statistics in harmonic and real space, we explore the expected consistency of Year 3 cosmic shear data from the Dark Energy Survey and how similar discrepancies can arise. We suggest several scale cuts and a method to test them, which we apply to the forthcoming analysis of DES Y3. To do so, we generate 500 mocks of a DES Y3-like survey from Gaussian simulations, which we analyze using a fast importance sampling method with various scale cuts, in order to measure the discrepancies that can be expected from pure statistical fluctuations in parameter space versus that originating in systematic effects.

Our findings are:

• We motivate two new methods to determine small-scale cuts from theory, both readily applicable to harmonic and real space two-point statistics; one is based on a three-dimensional k-mode cut-off, the other on a χ^2 distance between alternative predictions for the data vectors, here applied to the baryonic feedback model (which is the most conservative cut we test). We also use DES Y1 cuts, converted with $\ell \sim \pi/\theta$.

• Given our DES Y3 setup, we find that $\sigma(\Delta\widehat{S_8})$, the scatter of the difference $\Delta\widehat{S_8}$ between posterior means from harmonic and real space analyses, is of order 0.08−0.14. Its value is a fraction ~ 0.6−0.9 of the scatter for individual statistics (it would be $\sqrt{2} \approx 1.4$ for independent estimators). The correlation coefficient between $\widehat{S_8}|_{C_\ell}$ and $\widehat{S_8}|_{\xi_\pm}$ is highly sensitive to the choice of scale

cut, decreasing with more conservative cuts. Among the scale cuts we try, the $k_{\rm max}$-based scale cuts yield the best consistency metrics. In particular they lead to symmetric scatter in the two statistics and to a high correlation coefficient (86% for $k_{\rm max} = 3\,h\,{\rm Mpc}^{-1}$).

• We estimate the differential bias in S_8 due to a variety of systematics and modeling choices and we do not find, overall, one statistic to be intrinsically more biased than the other. Biases are generally small in our DES Y3-like setup and our proposed cuts, leading to shifts of less than a third of the statistical uncertainty. The partial exceptions are intrinsic alignment mechanism including tidal torquing (and redshift dependence) and baryonic feedback processes, especially for σ_8 and $\Omega_{\rm m}$. We conclude that our proposed cuts are immune to systematics tested here and are good candidates for the upcoming analysis for DES Y3, and easily adaptable to other surveys' characteristics.

• Our results indicate that with deeper surveys, and lower statistical errors, the biases due to systematics will be more significant—harmonic and real space statistics could then lead to different results in S_8 and other parameters. Extrapolating our results to LSST, with an effective number density of $30\,{\rm gal/arcmin^2}$ and area of $18\,000\,{\rm deg^2}$ (following Chang et al. 2013), error bars in the noise-dominated regime would reduce by ~ 4.3, so one might expect $\sigma(\Delta\widehat{S_8}) \sim 0.002$.

Although the trends observed for various scale cuts match our expectations, the numerical value of the scatter $\sigma(\widehat{S_8}|_{C_\ell} - \widehat{S_8}|_{\xi_\pm})$ is a complex function of scale cuts, survey characteristics and modeling, thus requiring simulations to quantify. We tested the impact of a number of systematic effects and alternatives in the ingredients of our baseline model, including non-linear power spectrum, baryonic feedback, intrinsic alignments, PSF leakage and redshift distribution uncertainty and found that the largest discrepancies are due to baryonic feedback, intrinsic alignments sourced by tidal torquing (TATT with $A_2 = -1$), particularly when redshift dependence is present but not modeled. This work will serve to guide the choice of small-scale cuts for the forthcoming analysis of DES Y3 cosmic shear data in harmonic space.

We also applied scale cuts used in the published HSC and KiDS-450 cosmic shear analyses and compared statistical and systematic differences in S_8, σ_8 and $\Omega_{\rm m}$. Although we used simulations with DES Y3-like characteristics, preventing us from drawing conclusions about observed spread, we do highlight some of our findings. We find a very low correlation of S_8 estimators when using HSC cuts, consistent with results of Hamana et al. (2020). Therefore the scatter of individual estimators $\widehat{S_8}$ is typically smaller than the scatter of the difference. For KiDS-450 cuts, we find asymmetric results, with the two-point functions measurements yielding higher S_8 than power spectra (as a matter of fact, closer to the truth because of a projection effect). It is finally worth noting that all systematic effects we tested point in the direction where $\widehat{\sigma_8}|_{C_\ell} > \widehat{\sigma_8}|_{\xi_\pm}$ (and $\widehat{\Omega_{\rm m}}|_{C_\ell} < \widehat{\Omega_{\rm m}}|_{\xi_\pm}$) for HSC, consistent with observations, although with modest but non-negligible amplitudes, typically of a fraction of the statistical spread. This indicates that no single systematic effect we test can create a significant differential bias, while a combination of effects could create differences of order $\sim 1\sigma$. Recent KiDS-1000 results compared three different statistics—two-point functions $\xi_\pm$, band powers of C_ℓ, COSEBIs (Complete Orthogonal Sets of E-/B-mode Integrals, Schneider et al. 2010)—and found them to be consistent (Asgari et al. 2020b), although all of them rely on initial $\xi_\pm$ measurements for thin bins in θ in the range 0.5−300′, corresponding to band powers from $\ell = 100$ to 1500. Scale cuts

were unchanged for $\xi_{\pm}$ and no cuts were applied to band powers or COSEBIs.

For future surveys, such as LSST, Euclid and Roman, those systematic shifts are expected to remain the same while statistical scatter will decrease with either higher depth or increased area, making control of those effects all the more important. We also note that we restricted the analysis to a single choice of estimator for each statistic, namely a pseudo-C_ℓ estimator of the shear power spectrum and the standard, unweighted estimator of the correlation functions $\xi_{\pm}(\theta)$ (Bartelmann & Schneider 2001). For each statistic, different estimators exist (Bond et al. 1998; Hikage et al. 2011) as well as alternative two-point statistics (*e.g.* the variance of the aperture mass statistic Schneider 1996), with various trade-off between computational difficulty and sensitivity to systematic effects. However, we have shown that scale cuts appear to be the key factor in terms of consistency between harmonic and real space, and we do not expect results would change in that regard. Nonetheless, some of these estimators were developed along with mitigation strategies to minimize biases from systematic effects (including deprojection of systematic templates for pseudo-C_ℓ, Elsner et al. 2017; Alonso et al. 2019; Weaverdyck & Huterer 2020), which would impact this part of our results, although this is beyond the scope of this paper. One could also imagine combining both harmonic and real space statistics into a joint analysis, provided that one can model the joint likelihood (in particular the cross-covariance). In other words, if constraints derived from the two statistics independently are not fully correlated, a joint analysis could capture extra information with respect to independent analyses. That information likely lies within the particular k-modes that are captured by one statistics and missed by the other, as discussed in the introduction. An alternative is to use other statistics that exploit information from both spaces, such as COSEBIs or Ψ- and Υ-statistics (Asgari et al. 2020a), at the cost of increased complexity in estimation from data and modeling from theory.

DATA AVAILABILITY

A general description of DES data releases is available on the survey website at `https://www.darkenergysurvey.org/the-des-project/data-access/`. DES Y1 cosmological data is available on the DES Data Management website hosted by the National Center for Supercomputing Applications at `https://des.ncsa.illinois.edu/releases/y1a1`. This includes the redshift distributions used in this analysis. DES-Y3 data will be made available at `https://des.ncsa.illinois.edu/releases`. The CosmoSIS software (Zuntz et al. 2015) is available at `https://bitbucket.org/joezuntz/cosmosis/wiki/Home`.

ACKNOWLEDGEMENTS

REFERENCES

Aihara H., et al., 2018a, PASJ, 70, S4
Aihara H., et al., 2018b, PASJ, 70, S8
Akeson R., et al., 2019, arXiv e-prints, p. arXiv:1902.05569
Albrecht A., et al., 2006, arXiv e-prints, pp astro–ph/0609591
Alonso D., Sanchez J., Slosar A., LSST Dark Energy Science Collaboration 2019, MNRAS, 484, 4127
Asgari M., Friswell I., Yoon M., Heymans C., Dvornik A., Joachimi B., Simon P., Zuntz J., 2020a, arXiv e-prints, p. arXiv:2004.07811
Asgari M., et al., 2020b, arXiv e-prints, p. arXiv:2007.15633
Barreira A., Krause E., Schmidt F., 2018, J. Cosmology Astropart. Phys., 2018, 053
Bartelmann M., Schneider P., 2001, Phys. Rep., 340, 291
Blazek J. A., MacCrann N., Troxel M. A., Fang X., 2019, Phys. Rev. D, 100, 103506
Bond J. R., Jaffe A. H., Knox L., 1998, Phys. Rev. D, 57, 2117
Bouhlel M. A., Hwang J. T., Bartoli N., Lafage R., Morlier J., Martins J. R. R. A., 2019, Advances in Engineering Software, p. 102662
Bridle S., King L., 2007, New Journal of Physics, 9, 444
Bridle S. L., Crittenden R., Melchiorri A., Hobson M. P., Kneissl R., Lasenby A. N., 2002, MNRAS, 335, 1193
Brown M. L., Taylor A. N., Hambly N. C., Dye S., 2002, MNRAS, 333, 501
Buchs R., Davis C., et al., 2019, MNRAS, 489, 820
Catelan P., Kamionkowski M., Blandford R. D., 2001, MNRAS, 320, L7
Chang C., et al., 2013, MNRAS, 434, 2121
Chisari N. E., et al., 2018, MNRAS, 480, 3962
Crittenden R. G., Natarajan P., Pen U.-L., Theuns T., 2001, ApJ, 559, 552
DES Collaboration et al., 2018, Phys. Rev. D, 98, 043526
Dias Pinto Vitenti S., Penna-Lima M., 2014, NumCosmo: Numerical Cosmology (ascl:1408.013)
Doux C., Penna-Lima M., Vitenti S. D. P., Tréguer J., Aubourg E., Ganga K., 2018, MNRAS, 480, 5386

[8] `https://numcosmo.github.io/`

Elsner F., Leistedt B., Peiris H. V., 2017, MNRAS, 465, 1847
Feroz F., Hobson M. P., Bridges M., 2009, MNRAS, 398, 1601
Flaugher B., 2005, International Journal of Modern Physics A, 20, 3121
Friedrich O., et al., 2020, in prep.
Gatti M., Sheldon E., et al., 2020, arXiv e-prints, p. arXiv:2011.03408
Górski K. M., Hivon E., Banday A. J., Wand elt B. D., Hansen F. K., Reinecke M., Bartelmann M., 2005, ApJ, 622, 759
Hamana T., et al., 2020, PASJ, 72, 16
Harnois-Déraps J., van Waerbeke L., Viola M., Heymans C., 2015, MNRAS, 450, 1212
Heitmann K., et al., 2016, ApJ, 820, 108
Heymans C., et al., 2006, MNRAS, 368, 1323
Heymans C., et al., 2020, arXiv e-prints, p. arXiv:2007.15632
Hikage C., Takada M., Hamana T., Spergel D., 2011, MNRAS, 412, 65
Hikage C., et al., 2019, PASJ, 71, 43
Hildebrandt H., et al., 2017, MNRAS, 465, 1454
Hirata C. M., Seljak U., 2004, Phys. Rev. D, 70, 063526
Howlett C., Lewis A., Hall A., Challinor A., 2012, J. Cosmology Astropart. Phys., 2012, 027
Hunter J. D., 2007, Computing in Science & Engineering, 9, 90
Huterer D., 2002, Phys. Rev. D, 65, 063001
Huterer D., Takada M., Bernstein G., Jain B., 2006, MNRAS, 366, 101
Ivezić Ž., et al., 2019, ApJ, 873, 111
Jain B., Seljak U., 1997, ApJ, 484, 560
Jarvis M., Bernstein G., Jain B., 2004, MNRAS, 352, 338
Jarvis M., et al., 2016, MNRAS, 460, 2245
Jarvis M., et al., 2020, arXiv e-prints, p. arXiv:2011.03409
Jin R., Chen W., Sudjianto A., 2005, Journal of Statistical Planning and Inference, 134, 268
Joachimi B., et al., 2020, arXiv e-prints, p. arXiv:2007.01844
Jones E., Oliphant T., Peterson P., et al., 2001–, SciPy: Open source scientific tools for Python, http://www.scipy.org/
Joudaki S., et al., 2018, MNRAS, 474, 4894
Kaiser N., 1992, ApJ, 388, 272
Kaiser N., 1998, ApJ, 498, 26
Kilbinger M., et al., 2013, MNRAS, 430, 2200
Kitching T. D., Alsing J., Heavens A. F., Jimenez R., McEwen J. D., Verde L., 2017, MNRAS, 469, 2737
Köhlinger F., et al., 2017, MNRAS, 471, 4412
Krause E., et al., 2017, arXiv e-prints, p. arXiv:1706.09359
Kuijken K., et al., 2015, MNRAS, 454, 3500
Lam S. K., Pitrou A., Seibert S., 2015, in Proceedings of the Second Workshop on the LLVM Compiler Infrastructure in HPC. LLVM '15. Association for Computing Machinery, New York, NY, USA, doi:10.1145/2833157.2833162, https://doi.org/10.1145/2833157.2833162
Laureijs R., et al., 2012, in Space Telescopes and Instrumentation 2012: Optical, Infrared, and Millimeter Wave. p. 84420T, doi:10.1117/12.926496
Lawrence E., et al., 2017, ApJ, 847, 50
Lemos P., Challinor A., Efstathiou G., 2017, J. Cosmology Astropart. Phys., 2017, 014
Lewis A., 2019, GetDist: MCMC sample analysis, plotting and GUI, https://github.com/cmbant/getdist
Lewis A., Challinor A., Lasenby A., 2000, ApJ, 538, 473
Limber D. N., 1953, ApJ, 117, 134
Liu J., Petri A., Haiman Z., Hui L., Kratochvil J. M., May M., 2015, Phys. Rev. D, 91, 063507
LoVerde M., Afshordi N., 2008, Phys. Rev. D, 78, 123506
Lu T., Haiman Z., 2019, MNRAS, 490, 5033
MacCrann N., Zuntz J., Bridle S., Jain B., Becker M. R., 2015, MNRAS, 451, 2877
Mackey J., White M., Kamionkowski M., 2002, MNRAS, 332, 788
Oliphant T. E., 2006, A guide to NumPy. Trelgol Publishing, USA
Packham N., 2015, Wilmott, 2015, 60
Planck Collaboration et al., 2020, A&A, 641, A6
Samuroff S., et al., 2019, MNRAS, 489, 5453
Schaye J., et al., 2010, MNRAS, 402, 1536
Schneider P., 1996, MNRAS, 283, 837

Schneider P., Eifler T., Krause E., 2010, A&A, 520, A116
Schneider A., Teyssier R., Stadel J., Chisari N. E., Le Brun A. M. C., Amara A., Refregier A., 2019, J. Cosmology Astropart. Phys., 2019, 020
Sevilla-Noarbe I., et al., 2020, arXiv e-prints, p. arXiv:2011.03407
Skare Ø., Bølviken E., Holden L., 2003, Scandinavian Journal of Statistics, 30, 719
Smith R. E., et al., 2003, MNRAS, 341, 1311
Takahashi R., Sato M., Nishimichi T., Taruya A., Oguri M., 2012, ApJ, 761, 152
Taylor A. N., Kitching T. D., 2010, MNRAS, 408, 865
Troxel M. A., et al., 2018a, Phys. Rev. D, 98, 043528
Troxel M. A., et al., 2018b, MNRAS, 479, 4998
Waskom M., et al., 2014, seaborn: v0.5.0 (November 2014), doi:10.5281/zenodo.12710, https://doi.org/10.5281/zenodo.12710
Weaverdyck N., Huterer D., 2020, arXiv e-prints, p. arXiv:2007.14499
Zonca A., Singer L., Lenz D., Reinecke M., Rosset C., Hivon E., Gorski K., 2019, The Journal of Open Source Software, 4, 1298
Zuntz J., et al., 2015, Astronomy and Computing, 12, 45
Zuntz J., Sheldon E., et al., 2018, MNRAS, 481, 1149
de Jong J. T. A., et al., 2013, The Messenger, 154, 44
van Daalen M. P., Schaye J., Booth C. M., Dalla Vecchia C., 2011, MNRAS, 415, 3649
van Uitert E., et al., 2018, MNRAS, 476, 4662

APPENDIX A: ADDITIONAL PLOTS ON σ_8 AND $\Omega_{\rm m}$

Figures A1 and A2 show the equivalents of Figs. 9 and 13 for σ_8 and $\Omega_{\rm m}$, respectively.

AFFILIATIONS

[1] Department of Physics and Astronomy, University of Pennsylvania, Philadelphia, PA 19104, USA
[2] Department of Astronomy and Astrophysics, University of Chicago, Chicago, IL 60637, USA
[3] Kavli Institute for Cosmological Physics, University of Chicago, Chicago, IL 60637, USA
[4] Center for Cosmology and Astro-Particle Physics, The Ohio State University, Columbus, OH 43210, USA
[5] Institute of Physics, Laboratory of Astrophysics, École Polytechnique Fédérale de Lausanne (EPFL), Observatoire de Sauverny, 1290 Versoix, Switzerland
[6] Instituto de Física Teórica, Universidade Estadual Paulista, São Paulo, Brazil
[7] Laboratório Interinstitucional de e-Astronomia - LIneA, Rua Gal. José Cristino 77, Rio de Janeiro, RJ - 20921-400, Brazil
[8] Department of Astronomy/Steward Observatory, University of Arizona, 933 North Cherry Avenue, Tucson, AZ 85721-0065, USA
[9] Institut de Física d'Altes Energies (IFAE), The Barcelona Institute of Science and Technology, Campus UAB, 08193 Bellaterra (Barcelona) Spain
[10] Department of Applied Mathematics and Theoretical Physics, University of Cambridge, Cambridge CB3 0WA, UK
[11] Department of Physics, Carnegie Mellon University, Pittsburgh, Pennsylvania 15312, USA
[12] Department of Physics, Duke University Durham, NC 27708, USA
[13] Institute for Astronomy, University of Edinburgh, Edinburgh EH9 3HJ, UK
[14] Departamento de Física Matemática, Instituto de Física, Universidade de São Paulo, CP 66318, São Paulo, SP, 05314-970,
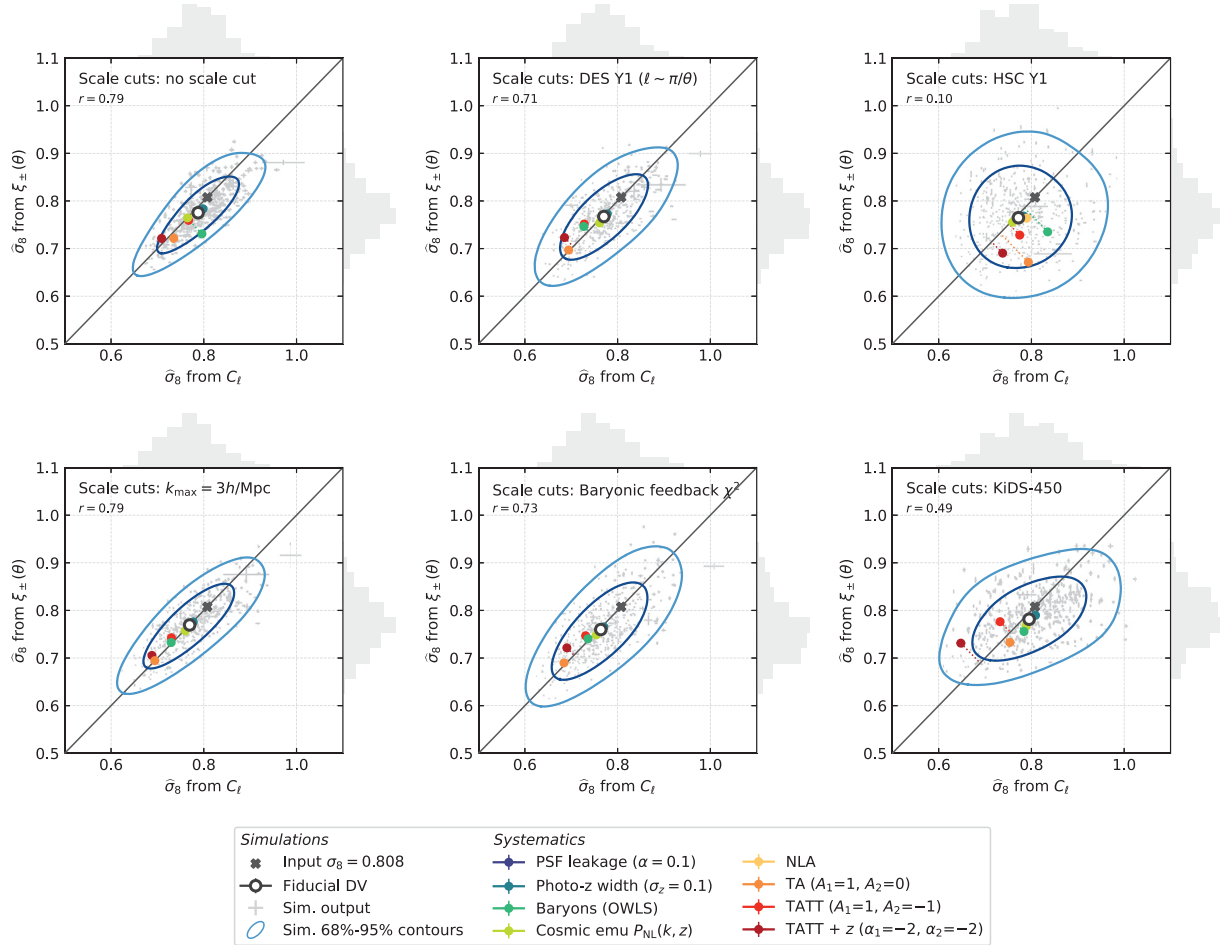
Figure A1. Same as Figs. 9 and 13 for σ_8.

Brazil

[15] Fermi National Accelerator Laboratory, P. O. Box 500, Batavia, IL 60510, USA

[16] Kavli Institute for Particle Astrophysics & Cosmology, P. O. Box 2450, Stanford University, Stanford, CA 94305, USA

[17] Instituto de Fisica Teorica UAM/CSIC, Universidad Autonoma de Madrid, 28049 Madrid, Spain

[18] Institute of Cosmology and Gravitation, University of Portsmouth, Portsmouth, PO1 3FX, UK

[19] CNRS, UMR 7095, Institut d'Astrophysique de Paris, F-75014, Paris, France

[20] Sorbonne Universités, UPMC Univ Paris 06, UMR 7095, Institut d'Astrophysique de Paris, F-75014, Paris, France

[21] Department of Physics & Astronomy, University College London, Gower Street, London, WC1E 6BT, UK

[22] SLAC National Accelerator Laboratory, Menlo Park, CA 94025, USA

[23] Instituto de Astrofisica de Canarias, E-38205 La Laguna, Tenerife, Spain

[24] Universidad de La Laguna, Dpto. Astrofísica, E-38206 La Laguna, Tenerife, Spain

[25] Center for Astrophysical Surveys, National Center for Supercomputing Applications, 1205 West Clark St., Urbana, IL 61801,

USA

[26] Department of Astronomy, University of Illinois at Urbana-Champaign, 1002 W. Green Street, Urbana, IL 61801, USA

[27] Astronomy Unit, Department of Physics, University of Trieste, via Tiepolo 11, I-34131 Trieste, Italy

[28] INAF-Osservatorio Astronomico di Trieste, via G. B. Tiepolo 11, I-34143 Trieste, Italy

[29] Institute for Fundamental Physics of the Universe, Via Beirut 2, 34014 Trieste, Italy

[30] Institut d'Estudis Espacials de Catalunya (IEEC), 08034 Barcelona, Spain

[31] Institute of Space Sciences (ICE, CSIC), Campus UAB, Carrer de Can Magrans, s/n, 08193 Barcelona, Spain

[32] Observatório Nacional, Rua Gal. José Cristino 77, Rio de Janeiro, RJ - 20921-400, Brazil

[33] Department of Physics, University of Michigan, Ann Arbor, MI 48109, USA

[34] School of Mathematics and Physics, University of Queensland, Brisbane, QLD 4072, Australia

[35] Faculty of Physics, Ludwig-Maximilians-Universität, Scheinerstr. 1, 81679 Munich, Germany

[36] Institute of Theoretical Astrophysics, University of Oslo. P.O. Box 1029 Blindern, NO-0315 Oslo, Norway
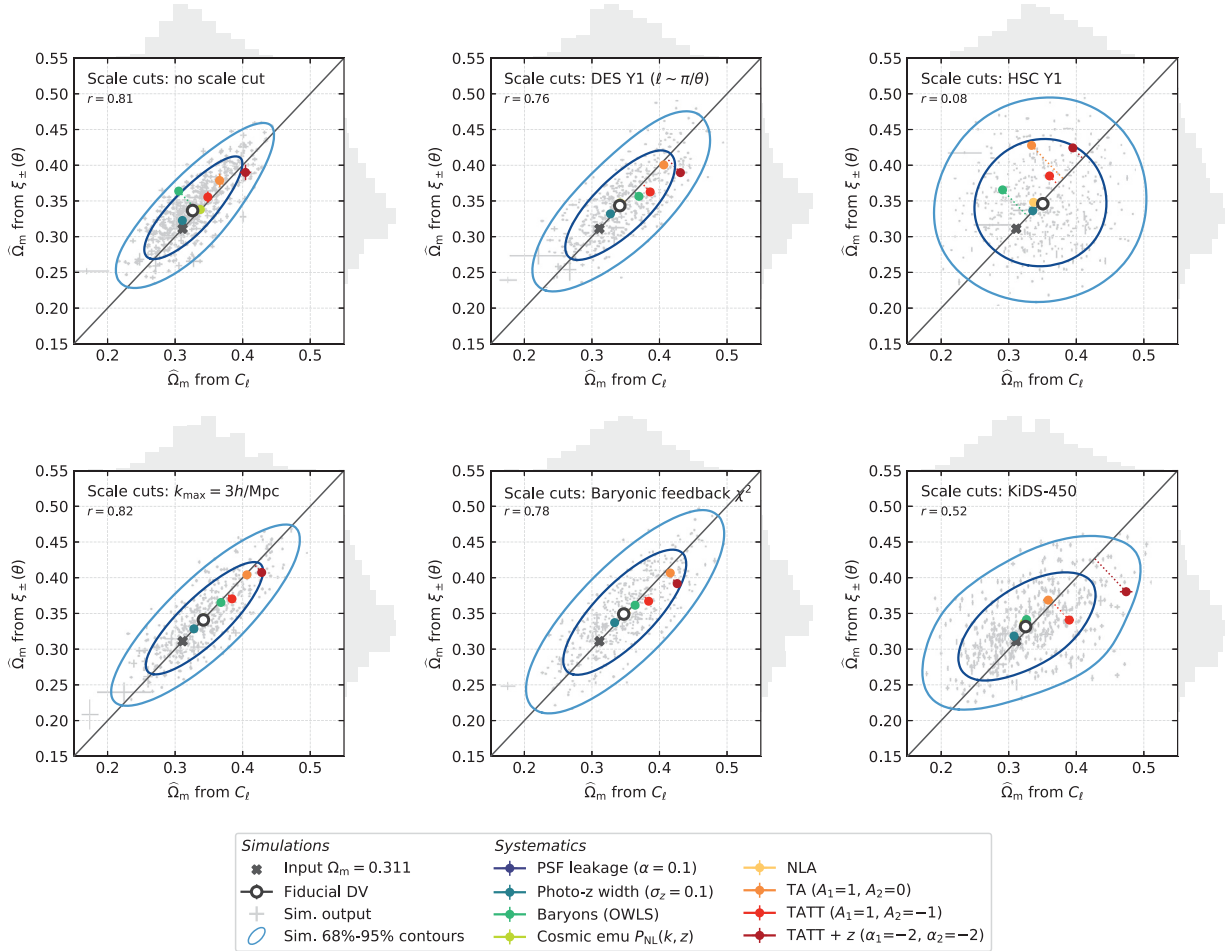
Figure A2. Same as Figs. 9 and 13 for Ω_{m}.

[37] Jet Propulsion Laboratory, California Institute of Technology, 4800 Oak Grove Dr., Pasadena, CA 91109, USA

[38] Department of Astronomy, University of Michigan, Ann Arbor, MI 48109, USA

[39] Department of Physics, Stanford University, 382 Via Pueblo Mall, Stanford, CA 94305, USA

[40] Département de Physique Théorique and Center for Astroparticle Physics, Université de Genève, 24 quai Ernest Ansermet, CH-1211 Geneva, Switzerland

[41] Santa Cruz Institute for Particle Physics, Santa Cruz, CA 95064, USA

[42] Center for Astrophysics | Harvard & Smithsonian, 60 Garden Street, Cambridge, MA 02138, USA

[43] Australian Astronomical Optics, Macquarie University, North Ryde, NSW 2113, Australia

[44] Lowell Observatory, 1400 Mars Hill Rd, Flagstaff, AZ 86001, USA

[45] George P. and Cynthia Woods Mitchell Institute for Fundamental Physics and Astronomy, and Department of Physics and Astronomy, Texas A&M University, College Station, TX 77843, USA

[46] Institució Catalana de Recerca i Estudis Avançats, E-08010 Barcelona, Spain

[47] Physics Department, 2320 Chamberlin Hall, University of Wisconsin-Madison, 1150 University Avenue Madison, WI 53706-1390

[48] Institute of Astronomy, University of Cambridge, Madingley Road, Cambridge CB3 0HA, UK

[49] Department of Astrophysical Sciences, Princeton University, Peyton Hall, Princeton, NJ 08544, USA

[50] Centro de Investigaciones Energéticas, Medioambientales y Tecnológicas (CIEMAT), Madrid, Spain

[51] School of Physics and Astronomy, University of Southampton, Southampton, SO17 1BJ, UK

[52] Computer Science and Mathematics Division, Oak Ridge National Laboratory, Oak Ridge, TN 37831

[53] Max Planck Institute for Extraterrestrial Physics, Giessenbachstrasse, 85748 Garching, Germany

[54] Universitäts-Sternwarte, Fakultät für Physik, Ludwig-Maximilians Universität München, Scheinerstr. 1, 81679 München, Germany

[55] Department of Physics and Astronomy, Pevensey Building, University of Sussex, Brighton, BN1 9QH, UK

This paper has been typeset from a TeX/LaTeX file prepared by the author.